Pressure and Composition Effects on Sound Velocity and Density of Core Forming Liquids: Implication to Core Compositions of Terrestrial Planets

Correspondence to:
H. Terasaki,
terasaki@ess.sci.osaka-u.ac.jp

Author Contributions:
Conceptualization: Hidenori Terasaki
Formal analysis: Hidenori Terasaki
Investigation: Hidenori Terasaki
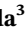**Methodology:** Keisuke Nishida
Writing - original draft: Hidenori Terasaki, Keisuke Nishida

Pressure and Composition Effects on Sound Velocity and Density of Core-Forming Liquids: Implication to Core Compositions of Terrestrial Planets

Hidenori Terasaki[1], Attilio Rivoldini[2], Yuta Shimoyama[1], Keisuke Nishida[3], Satoru Urakawa[4], Mayumi Maki[1], Fuyuka Kurokawa[1], Yusaku Takubo[1], Yuki Shibazaki[5,6], Tatsuya Sakamaki[7], Akihiko Machida[8], Yuji Higo[9], Kentaro Uesugi[9], Akihisa Takeuchi[9], Tetsu Watanuki[8], and Tadashi Kondo[1]

[1]Department of Earth and Space Science, Osaka University, Osaka, Japan, [2]Royal Observatory of Belgium, Brussels, Belgium, [3]Department of Earth and Planetary Science, The University of Tokyo, Tokyo, Japan, [4]Department of Earth Science, Okayama University, Okayama, Japan, [5]Frontier Research Institute for Interdisciplinary Sciences, Tohoku University, Sendai, Japan, [6]Now at International Center for Young Scientists, National Institute for Materials Science, Ibaraki, Japan, [7]Department of Earth Science, Tohoku University, Sendai, Japan, [8]Synchrotron Radiation Research Center, National Institutes for Quantum and Radiological Science and Technology, Hyogo, Japan, [9]Japan Synchrotron Radiation Research Institute, Hyogo, Japan

Abstract A compositional variety of planetary cores provides insight into their core/mantle evolution and chemistry in the early solar system. To infer core composition from geophysical data, a precise knowledge of elastic properties of core-forming materials is of prime importance. Here, we measure the sound velocity and density of liquid Fe-Ni-S (17 and 30 at% S) and Fe-Ni-Si (29 and 38 at% Si) at high pressures and report the effects of pressure and composition on these properties. Our data show that the addition of sulfur to iron substantially reduces the sound velocity of the alloy and the bulk modulus in the conditions of this study, while adding silicon to iron increases its sound velocity but has almost no effect on the bulk modulus. Based on the obtained elastic properties combined with geodesy data, S or Si content in the core is estimated to 4.6 wt% S or 10.5 wt% Si for Mercury, 9.8 wt% S or 18.3 wt% Si for the Moon, and 32.4 wt% S or 30.3 wt% Si for Mars. In these core compositions, differences in sound velocity profiles between an Fe-Ni-S and Fe-Ni-Si core in Mercury are small, whereas for Mars and the Moon, the differences are substantially larger and could be detected by upcoming seismic sounding missions to those bodies.

Plain Language Summary To estimate core compositions of terrestrial planets using geophysical data with high-pressure physical property of core-forming materials, we measure the sound velocity and density of liquid Fe-Ni-S and Fe-Ni-Si at high pressures. The effect of S and Si on elastic properties are quite different in the present conditions. Based on the obtained physical properties combined with geodesy data, S or Si content in the core of Mercury, Moon, and Mercury are estimated. In these core compositions, differences in sound velocity profiles between an Fe-Ni-S and Fe-Ni-Si core in Mars and the Moon are substantially large and could be detected by upcoming seismic sounding mission to Mars.

1. Introduction

Mercury, Mars, and Earth's moon (the Moon) are reported, from geophysical observations, to have a liquid core (Margot et al., 2007; Williams et al., 2001; Yoder et al., 2003). These planetary bodies are thought to have a core that mainly consists of Fe-5 ~ 10 wt% Ni and of some fractions of light elements (LEs; S, Si, O, C, and H; Dreibus & Wänke, 1985; Smith et al., 2012; Steenstra et al., 2016). Thus, the core is one of the major reservoirs of LEs in planetary body. Knowledge of the composition of the core of terrestrial planets is important not only for inferring the internal structure and thermal state of a planet, which strongly influence the core/mantle dynamics and their evolution, but also for understanding the distribution of LE in the solar nebula of the inner solar system (e.g., Rubie et al., 2015). To obtain constraints on the core composition, sound velocity and density of liquid Fe-alloys measured under planetary core conditions are indispensable information together with geodesy and geophysical data, such as mean density, moment of inertia, tidal Love number, and seismic wave velocity.
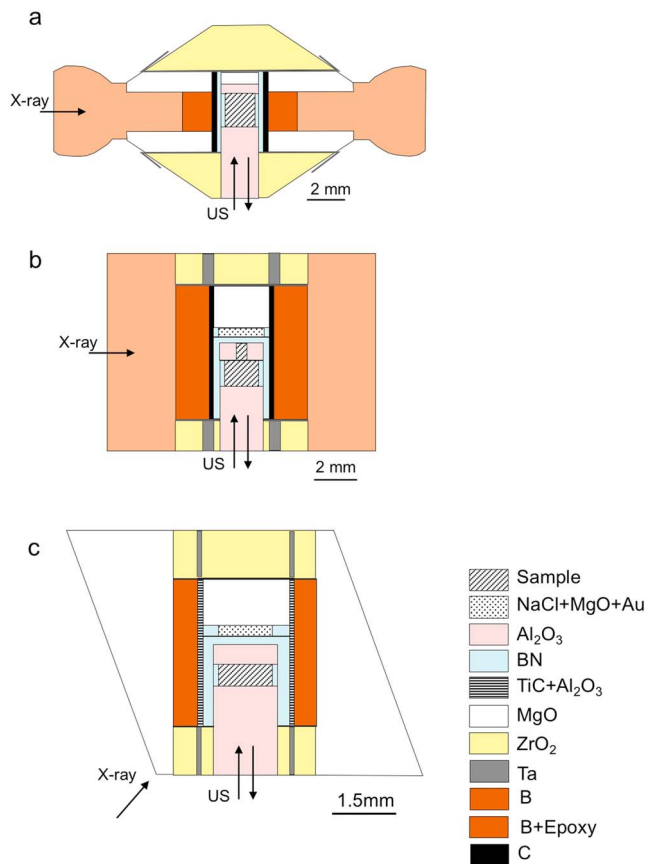
Figure 1. Schematic illustrations of used cell assemblies. A monochromatic X-ray passes horizontally through the center of the cell. The ultrasonic signal (US) comes from the bottomside of the cell as shown by arrows. (a) Cupped-type cell used for $P < 1$ GPa at BL20XU. (b) Cell assembly of cubic-type multianvil press used for $1 < P < 5$ GPa at BL22XU. (c) Cell assembly of Kawai-type multianvil press used for $P > 5$ GPa at BL04B1.

S and Si are known to be the major candidates as the LEs in planetary cores, as they have high solar abundance (Palme & Jones, 2005) and are present in primordial meteorites. Fe-Ni-S is widely found in chondrites and iron meteorites (Mittlefehldt et al., 1998), and Fe-Ni-Si is found in enstatite chondrites (Brearley & Jones, 1998), which are one of the candidate building blocks for the Earth (Javoy et al., 2010), Mars (Sanloup et al., 1999), and Mercury (Wasson, 1989). Because the solubility of S and Si in liquid Fe strongly depends on the oxygen fugacity conditions in the planetary interiors (Malavergne et al., 2010), identifying the core LEs also provides information about the redox environment inside the planet.

Recently, the compressional wave velocities (V_P) of liquid Fe-Ni, Fe-S, and Fe-C have been measured in static high-pressure experiments. These results show that S, C, and Ni reduce the V_P of liquid Fe at pressures below 10 GPa (Jing et al., 2014; Kuwabara et al., 2016; Nishida et al., 2013, 2016; Shimoyama et al., 2016), while S and C increase the V_P of liquid Fe above 10 GPa (Kawaguchi et al., 2017; Nakajima et al., 2015). To explain these trends, a possible change in the structure and electronic properties of liquid Fe-S is thought to occur at around 10 GPa (Kawaguchi et al., 2017). However, these two opposing trends were obtained by different methods, that is, ultrasonic method below 10 GPa and inelastic X-ray scattering (IXS) method above 10 GPa. To ascertain the exact elastic behavior, V_P data should be measured using the same method in wide pressure range, especially below and above 10 GPa. In addition, V_P measurements at high-pressure for liquid Fe-Ni-Si, an important candidate for the core material, has never been reported.

In this paper, we investigate the effects of pressure, temperature, and LEs (S and Si) on the sound velocity and density of potential core-forming liquids (Fe-Ni-S and Fe-Ni-Si) by using the ultrasonic pulse-echo overlap method and the X-ray absorption method. Then, the core compositions of Mercury, the Moon, and Mars are estimated based on the obtained elastic properties, in conjunction with geodesy data, and hence we propose the seismic wave velocity and density profiles of these bodies.

2. Methods

2.1. Sample Compositions

The sample compositions used were $Fe_{73}Ni_{10}S_{17}$ in at% (S = 10.5 wt%) and $Fe_{60}Ni_{10}S_{30}$ (S = 19.6 wt%) for liquid Fe-Ni-S, and $Fe_{61}Ni_{10}Si_{29}$ (Si = 16.9 wt%) and $Fe_{52}Ni_{10}Si_{38}$ (Si = 23.4 wt%) for liquid Fe-Ni-Si. These were composed of a mixture of powdered Fe, Ni (both were 99.99%) and FeS (99.9%) or FeSi (99.9%). The pelleted sample was enclosed in a hexagonal-BN cylinder. The top and bottom of the sample pellet were sandwiched by a mirror-polished single crystal sapphire buffer rod and a backing plate (Figure 1).

2.2. High-Pressure Experiments

High pressure was generated using three different high-pressure apparatuses generating different pressure ranges. The sound velocity was measured using the ultrasonic pulse-echo overlapping method. The density was measured using the X-ray absorption method based on the Beer-Lambert law or using the X-ray computed tomography (CT) measurement. For the measurements below 1 GPa, an 80-ton portable uniaxial press (Urakawa et al., 2010) was used combined with X-ray computed-tomography (CT) measurements (Kuwabara et al., 2016) at the BL20XU beamline, SPring-8 synchrotron radiation facility in Japan. High pressure was generated using opposing cupped WC anvils (diameter of the center cup was 12 mm) with a ringed groove. The cell assembly was a toroidal type as shown in Figure 1a. For the measurements from 1 to 5 GPa, we used a 180-ton cubic-type multianvil press at BL22XU beamline, SPring-8 (Shimoyama et al., 2016). The truncated edge length of the tungsten carbide anvil was 6 mm. We used two different sample diameters in
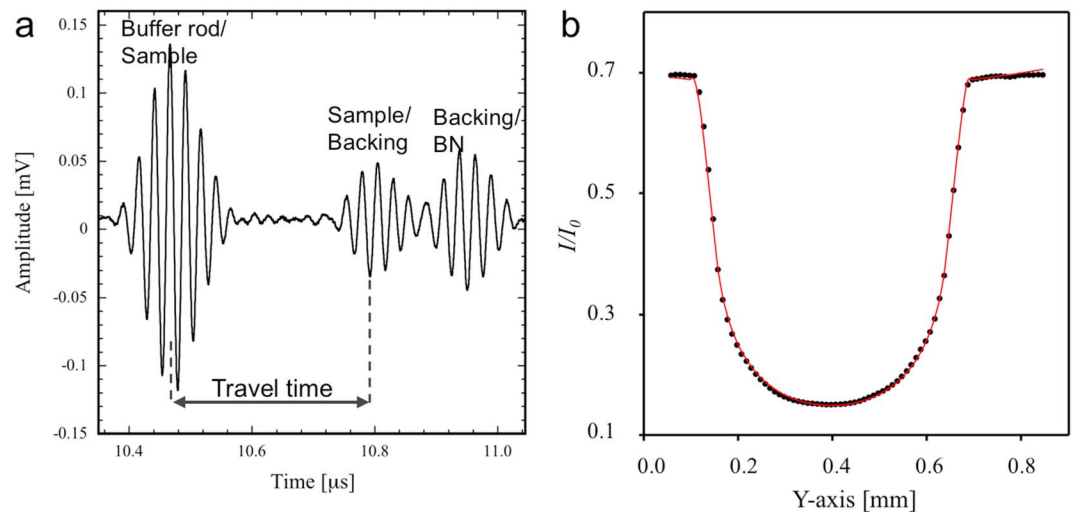
Figure 2. (a) Echo signal of the liquid $Fe_{73}Ni_{10}S_{17}$ sample obtained at 2.8 GPa and 1600 K. The three sinusoidal signals correspond to echoes at the Fe-Ni-S sample front (buffer rod/sample), sample back (sample/backing plate), and backing plate/BN, respectively (see the assembly in Figure 1b). The time between the sample front and the back corresponds to the two-way travel time in the sample, as indicated by an arrow. (b) X-ray absorption profile of the liquid $Fe_{73}Ni_{10}S_{17}$ at 2.8 GPa and 1600 K as a function of position on a horizontal axis (Y) perpendicular to the X-ray. Black circles and red curve denote raw data and fitted curve using the Beer-Lambert law, respectively.

the same cell (Figure 1b). The initial diameter of the sample for sound velocity measurement was 1.5 mm to obtain a clear echo signal from the sample interfaces and that for density measurement was 0.5 mm to obtain appropriate X-ray absorption contrast between the sample and surrounding materials. For measurements above 5 GPa, a 1,500-ton Kawai-type multianvil press was used at BL04B1 beamline, SPring-8 (Nishida et al., 2013). The truncated edge length of the 2nd stage tungsten carbide anvils was 5 mm. The cell assemblies used in this study are shown in Figure 1c.

Monochromatized X-rays (37.7 keV at BL20XU, 35 keV at BL22XU, and 51 keV at BL04B1), which were tuned by Si (111) or Si (311) double-crystal monochromators, were used (Shobu et al., 2007; Suzuki et al., 2004). The energies of the X-rays were optimized from the sample size to obtain appropriate X-ray absorption contrasts. The X-ray radiography image was obtained using a complementary metal-oxide semiconductor camera (ORCA-flash 4.0, Hamamatsu Photonics K. K., Japan) with an Yttrium Aluminium Garnet (YAG) scintillator.

The X-ray diffraction (XRD) spectra of the sample and pressure markers (MgO and hexagonal-BN for experiments at P < 5 GPa; MgO, NaCl and Au for experiments at P > 5 GPa) were collected using a complementary metal-oxide semiconductor flat panel detector (C7942-CA/C7942CK-12, Hamamatsu Photonics K. K.) to determine density of solid phases, and the experimental pressures and temperatures, respectively. Melting of the samples was identified by the disappearance of the XRD peaks and the appearance of a diffuse scattering signal. The experimental pressures and temperatures were obtained from the lattice volumes of a pair of pressure markers combined with their equations of state (MgO: Tange et al., 2009; hexagonal-BN: Wakabayashi & Funamori, 2015; NaCl: Matsui, 2009; Au: Tsuchiya, 2003). Difference in pressure and temperature between sample and pressure marker in the cell (Figure 1c) were checked by placing the pressure marker in the sample capsule instead of the sample. Both difference in pressure and temperature between the sample and pressure marker becomes to be quite small at higher temperature above 800 K (ΔP < 0.5 GPa and ΔT < 60 K).

2.3. Sound Velocity Measurement

Compressional wave velocity (V_P) was measured using the ultrasonic pulse-echo overlap method (Higo et al., 2009). A 10° Y-cut $LiNbO_3$ transducer was attached to the backside of the anvil to generate and receive compressional wave acoustic signals. Input electric signals of sine waves with frequencies of 35–45 MHz were generated using a waveform generator (AWG2021/AFG3251C/AWG710B, Tektronix Inc.).

AGU
100
ADVANCING EARTH
AND SPACE SCIENCE

Journal of Geophysical Research: Planets

10.1029/2019JE005936

Table 1
Experimental Conditions and Measured Sound Velocity and Density of Liquid Fe-Ni-S

Run no.	P (GPa)[a]	P error[b]	T (K)	V_P (m/s)	V_P error	ρ (g/cm^3)	ρ error
Fe$_{73}$Ni$_{10}$S$_{17}$							
B268	2.8	0.2	1600	3,530	20	6.18	0.04
	2.8	0.2	1720	3,540	20	6.19	0.05
B261	3.2	0.1	1900	3,650	20	6.13	0.03
	3.2	0.2	1970	3,700	10		
	3.2	0.2	2040	3,720	20	5.99	0.03
	3.1	0.1	2060	3,690	30		
	3.0	0.1	2080	3,690	30	6.05	0.03
B274	3.8	0.0	1680	4,040	80	6.37	0.05
	3.8	0.1	1760	3,990	60		
	3.9	0.2	1840	3,990	60		
	3.9	0.2	1890	3,930	50		
	3.9	0.3	1940	3,930	50	6.35	0.05
S3069	7.5	0.5	1830	4,370	140		
	7.2	0.5	2040	4,380	200		
	7.0	0.5	2150	4,310	280		
	7.0	0.5	2200	4,240	320		
S2991	10.0	0.1	1510	4,780	90		
	9.8	0.1	1570	4,830	100		
S3067	10.4	0.6	2100	4,890	290		
	10.5	0.6	2250	4,830	260		
	10.5	0.6	2250	4,660	250		
S3090	13.9	0.1	1610	4,950	180		
Fe$_{60}$Ni$_{10}$S$_{30}$							
B277	2.4	0.2	1660	3,120	10	5.65	0.02
	2.4	0.3	1740	3,130	10		
	2.5	0.3	1810	3,140	10	5.51	0.02
	2.3	0.5	1910	3,140	10		
B263	3.0	0.1	1620	3,240	20		
	3.1	0.1	1690	3,280	20	5.71	0.02
	3.1	0.1	1690	3,290	20	5.71	0.02
	3.1	0.1	1700	3,300	20		
	3.1	0.2	1890	3,310	20	5.58	0.02
	3.1	0.2	1890	3,310	10		
	3.0	0.3	1960	3,270	20		
	3.0	0.3	1960	3,270	20		
B275	3.4	0.0	1450			5.70	0.03
	3.4	0.0	1560	3,360	40		
	3.6	0.0	1640	3,390	40		
	3.8	0.0	1710	3,400	30		
S3070	7.3	0.7	1330	3,650	290		
	7.3	0.7	1410	3,700	260		
	7.4	0.6	1500	3,660	240		
	7.4	0.5	1580	3,730	260		
	7.5	0.4	1670	3,650	270		
S3068	10.4	0.1	1490	4,110	250		
	10.3	0.1	1520	4,160	250		
	10.3	0.1	1520	4,110	220		
	10.1	0.0	1580	4,160	220		
	9.8	0.0	1650	4,220	200		
	9.7	0.1	1700	4,090	200		
S3091	12.6	0.1	1240	4,310	120		
	12.4	0.1	1340	4,340	110		

[a]Used pressure marker pairs were BN+MgO: B268, 261, 274, 277, 263, 275; NaCl+MgO: S2991, 3067, 3090, 3070, 3068, 3091; NaCl+Au: S3069, 3067. [b]Pressure errors were derived from errors in lattice volumes of pressure markers.

Table 2

Experimental Conditions and Measured Sound Velocity and Density of Liquid Fe-Ni-Si

Run no.	P (GPa)[a]	P error[b]	T (K)	V_P (m/s)	V_P error	ρ (g/cm³)	ρ error
Fe₆₁Ni₁₀Si₂₉							
HPT26	0.3	0.04	2070	3,990	50		
HPT24	0.4	0.02	1590	4,070	30		
	0.3	0.02	1680	3,960	30		
B250	2.5	0.05	1680			6.37	0.03
	2.5	0.05	1730	4,360	90		
	2.5	0.05	1780	4,360	80	6.23	0.03
	2.5	0.00	1880	4,360	60		
	2.5	0.00	1970	4,290	80	6.17	0.04
B247	3.3	0.09	1950			6.24	0.04
	3.3	0.35	2020	4,510	170		
	3.3	0.22	2060	4,400	170		
B251	4.2	0.05	1790			6.32	0.06
	4.4	0.10	1840			6.34	0.06
	4.5	0.10	1880	4,600	40	6.32	0.06
	4.4	0.20	1890	4,610	50		
	4.3	0.29	1910			6.29	0.06
Fe₅₂Ni₁₀Si₃₈							
HPT23	0.5	0.12	1770	4,140	90		
	0.4	0.04	1910	4,180	330		
B282	2.1	0.13	1630	4,530	30		
	2.1	0.14	1690	4,500	30		
	2.1	0.14	1740	4,470	30		
B260	2.9	0.10	1830			5.87	0.03
	2.8	0.16	1860	4,450	60		
	2.7	0.22	1880				
	2.8	0.13	2090	4,430	60	5.60	0.03
B285	3.9	0.23	1970	4,540	20		
S3143	9.7	0.60	1690	5,150	100		
	10.0	0.54	1560	5,330	110		
	9.9	0.57	1630	5,220	110		
	9.5	0.63	1780	5,160	140		
	9.3	0.67	1870	5,080	110		
	9.1	0.71	1960	5,100	140		
	8.9	0.75	2060	5,030	100		
S3140	11.8	0.15	1900	5,350	140		
	11.9	0.15	1820	5,380	140		
	11.7	0.15	1980	5,300	140		
	11.5	0.15	2050	5,280	150		

Note. Used pressure marker pairs were BN+MgO: B250, 247, 251, 282, 260, 285; NaCl+MgO: S3143, 3140; BN³: HPT26, 24, 23. [a]*P* was estimated from EoS of BN and *T* was calibrated from separate run as described in Terasaki et al. (2019). [b]Pressure errors were derived from errors in lattice volumes of pressure markers.

The echo signals from the sample were detected using a high-resolution digital oscilloscope (DPO5054/DPO7104, Tektronix Inc.) with a sampling rate of 5×10^9 or 1×10^{10} points/s. The signal travel time in the sample was obtained from the time difference in the echo signals between the near and far sides of the sample interfaces. The length of the sample was measured from the X-ray radiography image (pixel size = 2.5–3.0 μm). The sample thickness ranges 330–745 μm below 10 GPa and 240–460 μm above 10 GPa. The V_P was calculated from the measured travel time and sample length. Details of travel time and sample length analyses are described elsewhere (Kono et al., 2012). A typical example of an echo signal from the sample interface is shown in Figure 2a. The error in V_P, listed in Tables 1 and 2, was derived mainly from estimated errors in sample length determination, which was caused mainly by clearness of image contrast and brightness and also by variation in sample length and from the travel time uncertainty caused by overlapping echo signals.

2.4. Density Measurement

The density was measured from the X-ray absorption method (Katayama, 1996) based on the Beer-Lambert law or from volume measurement using X-ray CT. For X-ray absorption method, a monochromatized X-ray was collimated to 50×50-μm size and introduced to the sample. Intensities of incident (I_0) and transmitted (I) X-rays, through the sample, were measured using two ion chambers located upstream and downstream of the press, respectively. The X-ray absorption (I/I_0) profile of the sample was obtained by scanning the press perpendicular to the X-ray direction with a 10-μm step. A typical example of an X-ray absorption profile of a liquid sample is shown in Figure 2b. The density (ρ) of the sample was obtained by fitting the X-ray absorption profile with the Beer-Lambert law,

$$I/I_0 = \exp(-\mu_s \rho_s t_s - \mu_e \rho_e t_e), \tag{1}$$

where μ and t denote mass absorption coefficient and thickness of X-ray absorbers, respectively. Subscripts s and e represent sample and surrounding materials, respectively. The μ of the sample, μ_s, can be determined from the solid sample density measured using XRD and its X-ray absorption profile. Then, the sample density, ρ_s, and thickness, t_s, were deduced by fitting the profile using equation (1). Details of this procedure were reported in previous study (Shimoyama et al., 2016). The density error, listed in Tables 1 and 2, was mainly derived from fitting error for the X-ray absorption profile using equation (1). For X-ray CT measurement, the volume of the sample was obtained from in situ 3-D image measured using X-ray CT. Details of the X-ray CT are given in Appendix A.

3. Results

The experimental conditions and obtained results are given in Tables 1 and 2. The compressional wave velocities (V_P) of liquid Fe-Ni-S (Fe₇₃Ni₁₀S₁₇ and Fe₆₀Ni₁₀S₃₀) and liquid Fe-Ni-Si (Fe₆₁Ni₁₀Si₂₉ and Fe₅₂Ni₁₀Si₃₈) are shown in Figures 3a and 3b. The V_P of liquid Fe-Ni-S increases nonlinearly and that of liquid Fe-Ni-Si increases more monotonously with pressure. The V_P of liquid Fe₇₃Ni₁₀S₁₇ is similar to that of liquid Fe₈₀S₂₀ (Nishida et al., 2016; open diamonds in Figure 3a), suggesting that the effect of Ni on the V_P of liquid Fe-S is small. The V_P of liquid Fe-Ni-S is less sensitive to temperature (see Table 1), which is
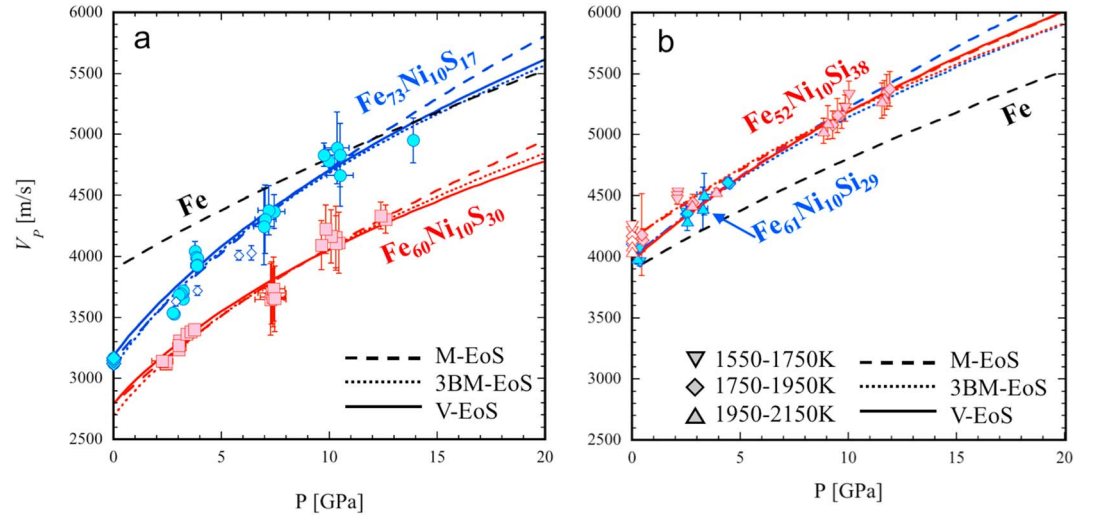
Figure 3. The effect of pressure on V_P. Dashed, dotted, and solid curves represent fittings using Murnaghan, third-order Brich-Murnaghan, and Vinet EoS, respectively. The V_P of liquid Fe are shown by black dashed (Jing et al., 2014). (a) Liquid Fe-Ni-S. Blue circles and red squares denote the V_P of $Fe_{73}Ni_{10}S_{17}$ and $Fe_{60}Ni_{10}S_{30}$, respectively. Open diamonds indicate reported V_P of liquid $Fe_{80}S_{20}$ (Nishida et al., 2016). As the effect of T on V_P is minor (see text), we plotted V_P at all T conditions. Data at ambient pressure are taken from Nasch et al. (1997). (b) Liquid Fe-Ni-Si. Blue and red symbols denote the V_P of $Fe_{61}Ni_{10}Si_{29}$ and $Fe_{52}Ni_{10}Si_{38}$, respectively. Different symbol shapes represent different temperatures as shown in the legend. Data at ambient pressure are taken from Williams et al. (2015).

consistent with previous results for liquid Fe-S (Jing et al., 2014; Nishida et al., 2013). On the other hand, the V_P of liquid Fe-Ni-Si decreases slightly with increasing temperature with dV_P/dT of -0.42 to -0.57 $ms^{-1} \cdot K^{-1}$ (see Table 2). The dV_P/dT found in this study is in agreement with that measured at ambient pressure (-0.36 to -0.52 $ms^{-1} \cdot K^{-1}$; Williams et al., 2015).

The V_P of a liquid is expressed using density (ρ) and adiabatic bulk modulus (K_S) as follows:

Table 3
Adiabatic Elastic Properties

Composition	EoS[a]	T_0 (K)	K_{S0} (GPa)	K_{S0} error	K'_S	K'_S error	ρ_0 [g/cm³]	ρ_0 error	α_0 (10⁻⁵/K)	α_0 error	dK_S/dT	dK_S/dT error	γ_0 (fix)	δ_{S0}[b]
$Fe_{73}Ni_{10}S_{17}$	M	1650	58.8	1.6	8.7	0.3	5.91	0.02						
	3BM	1650	56.2	3.5	11.2	0.4	5.91	0.02						
	V	1650	55.2	3.2	10.5	0.7	5.91	0.02	10.1	1.8	−0.01	0.001	2.30	1.8
$Fe_{60}Ni_{10}S_{30}$	M	1650	40.8	1.0	6.0	0.2	5.21	0.02						
	3BM	1650	38.1	1.8	7.4	0.2	5.21	0.02						
	V	1650	37.1	1.9	7.8	0.4	5.21	0.02	11.0	(fix)	−0.004	0.002	2.30	1.0
$Fe_{61}Ni_{10}Si_{29}$	M	1650	98.5	1.5	8.3	0.6	6.15	0.03						
	3BM	1650	97.9	2.3	8.8	0.5	6.15	0.03						
	V	1650	96.5	2.6	9.3	0.9	6.15	0.03	9.5	3.3	−0.015	0.010	1.73	1.6
$Fe_{52}Ni_{10}Si_{38}$	M	1550	101.9	1.3	7.0	0.2	5.95	0.07						
	3BM	1550	102.1	1.1	7.8	0.1	5.95	0.07						
	V	1550	108.4	4.1	7.1	0.5	5.95	0.07	20.4	4.0	−0.049	0.014	1.73	2.2
$Fe_{90}Ni_{10}$	M[c]	1900	103.0	2.0	5.7	0.8	6.97							
	3BM[c]	1900	103.1	1.7	6.0	0.1	6.97							
Fe	M[d]	1673	105.0	2.0	6.7	1.0	6.91							
	3BM[e]	1811	109.7	0.7	4.7	0.0	7.02							

Note. δ_S is given from α, K_S, and dK_S/dT using $\delta_S = -(1/\alpha K_S)(dK_S/dT)_P$.
[a]Abbreviations: M: Murnaghan EoS, 3BM: third-order Birch-Murnaghan EoS, V: Vinet EoS. [b]Note that $\delta_S = -(1/\alpha K_S)(dK_S/dT)_P$. [c]Kuwabara et al. (2016). [d]Jing et al. (2014). [e]Anderson & Ahrens (1994).

Table 4
Isothermal Elastic Properties

Composition	EoS[a]	T_0 (K)	K_{T0} (GPa)	K_{T0} error	K'_T	K'_T error	ρ_0 (g/cm^3)	ρ_0 error	α_0 (10^{-5}/K)	α_0 error	dK_T/dT	dK_T/dT error	γ_0 (fix)	δ_{T0}[b]
Fe$_{73}$Ni$_{10}$S$_{17}$	3BM	1650	40.7	1.4	10.6	0.3	5.91	0.02	10.0	1.8	−0.014	0.004	2.30	3.4
	V	1650	38.5	3.1	10.0	0.6	5.91	0.02	10.0	1.8	−0.014	0.004	2.30	3.6
Fe$_{60}$Ni$_{10}$S$_{30}$	3BM	1650	27.7	1.0	7.8	0.2	5.24	0.02	11.0	(fix)	−0.018	0.006	2.30	5.9
	V	1650	28.0	2.0	7.4	0.4	5.24	0.02	11.0	(fix)	−0.018	0.006	2.30	5.8
Fe$_{61}$Ni$_{10}$Si$_{29}$	3BM	1650	76.8	1.2	8.3	0.4	6.15	0.03	9.6	3.4	−0.022	0.011	1.73	3.0
	V	1650	75.9	6.1	8.6	1.0	6.15	0.03	9.6	3.4	−0.022	0.011	1.73	3.0
Fe$_{52}$Ni$_{10}$Si$_{38}$	3BM	1550	69.0	0.1	7.5	0.1	5.94	0.07	19.7	3.5	−0.050	0.010	1.73	3.7
	V	1550	70.0	4.0	7.1	0.4	5.94	0.07	19.7	3.5	−0.050	0.010	1.73	3.6

[a]Abbreviations: M: Murnaghan EoS, 3BM: third-order Birch-Murnaghan EoS, V: Vinet EoS. [b]Note that $\delta_T = -(1/\alpha K_T)(dK_T/dT)_P$. Note that α_0 and dK_T/dT of 3BM were used from those of Vinet EoS.

$$V_P(P,T) = \sqrt{\frac{K_S(P,T)}{\rho(P,T)}} \tag{2}$$

where ρ and K_S are expressed as function of pressure (P) and temperature (T) using equations of state (EoS). For the effect of pressure on the V_P, previous studies have assumed either a linear dependence of V_P on P (Nishida et al., 2013) or a Murnaghan EoS (Jing et al., 2014), where K_S is a linear function of P. In this study, we considered three types of EoS—Murnaghan EoS (M), third-order Birch-Murnaghan EoS (3BM), and Vinet EoS (V)—to assess the pressure dependence of V_P. The 3BM EoS is widely used for compression behavior of solid materials and the V EoS is reported to provide a more accurate description of compressional behavior for highly compressible materials, such as liquids (Cohen et al., 2000). The expressions for three EoS are given in Appendix B. The elastic properties (K_0 and K') have been obtained by fitting
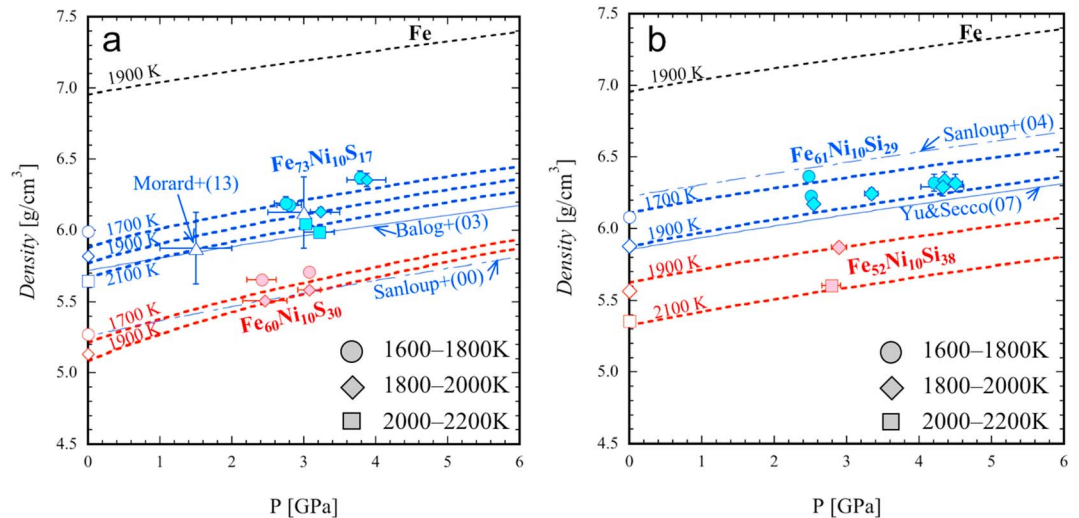

Figure 4. The effect of pressure on ρ. Different symbol shapes represent different temperatures as shown in the legend. Dashed curves indicate the calculated density from isothermal 3BM-EoS at different temperatures. The ρ of liquid Fe is shown by black dashed curve (Anderson & Ahrens, 1994). (a) Liquid Fe-Ni-S. Blue and red symbols denote the ρ of Fe$_{73}$Ni$_{10}$S$_{17}$ and Fe$_{60}$Ni$_{10}$S$_{30}$, respectively. The ρ_0 (density at ambient pressure) were taken from the data of Nagamori (1969). Open triangles indicate the ρ of liquid Fe$_{77.1}$S$_{22.9}$ (14.6 wt%S) at 1860 K reported by Morard, Garbarino, et al. (2013), Morard, Siebert, et al. (2013). Blue solid and dash-dotted curves respectively represent the ρ of liquid Fe$_{84}$S$_{16}$ (10 wt%S) at 1700 K reported by Balog et al. (2003) and that by Sanloup et al. (2000). (b) Liquid Fe-Ni-Si. Blue and red symbols denote the ρ of Fe$_{61}$Ni$_{10}$Si$_{29}$ and Fe$_{52}$Ni$_{10}$Si$_{38}$, respectively. The ρ_0 were taken from data of Kawai et al. (1974). Blue solid and dash-dotted curves, respectively, represent the ρ of liquid Fe$_{71}$Si$_{29}$ (17 wt%Si) at 1800 K reported by Yu and Secco (2008) and by Sanloup et al. (2004).

Table 5
EoS Parameters of End Members

Parameter	Fe[c]	FeS[d]	FeSi[e]
ρ_0 (g/cm^3)	7.019	3.725	5.103
K_{T0} (GPa)	85.1	18.3	69.0
K_{T}'	5.8	5.8	7.4
dK/dT (GPa/K)	−0.035	—	−0.042
δ_T [a]	—[b]	10.10	3.47
α_0 [10^{-5} K^{-1}]	—[b]	12.88	17.54
γ_0	1.4	1.4	1.6
T_0 [K]	1811	1650	1723

[a]δ_T is Anderson-Gruneisen parameter defined as $\alpha/\alpha_0 = (\rho_0/\rho)^{\delta_T}$.
[b]$\rho_0(T)$ (g/cm^3) = $[(1.3105 \times 10^{-5})(T - T_0) + 0.14247]^{-1}$.
[c]Anderson & Ahrens (1994). [d]Nagamori (1969); Kaiura & Toguri (1979); Nishida et al. (2016); Antonangeli et al. (2015). [e]Kawai et al. (1074); Dumay & Cramb (1995); Yu & Secco (2008); Williams et al. (2015).

the V_P and/or ρ data of Fe-Ni-S and Fe-Ni-Si liquids using the EoSs (equations (B1)–(B7) in Appendix B) with equation (2). Isentropic and isothermal elastic properties in Tables 3 and 4 are obtained independently from isentropic and isothermal fittings, respectively. Details of the isothermal and isentropic fittings are given in Appendix B. The errors of elastic properties are derived from fitting error, in which the errors of V_P and density data are also taken into account. The errors of all the obtained elastic properties are listed in Tables 3 and 4.

The measured V_P and the fitted EoS are shown in Figure 3. The 3BM- and V-EoS reproduce the V_P data well and show a similar trend within the pressure range of the experiments (Figures 3a and 3b). On the contrary, the M-EoS does not reproduce the V_P data adequately especially for liquid Fe-Ni-S. The calculated V_P using the M-EoS deviates from the measured V_P data and from the calculated V_P using the 3BM- or V-EoS at pressures greater than 10 GPa (Figure 3a). This can be attributed to the assumption in the M-EoS that K_S is a simple linear function of P [see equation (B2)].

Thus, the 3BM- or V-EoS fits are more appropriate to express the pressure dependence of V_P especially for compressible liquids such as Fe-Ni-S. These EoS can accurately link the V_P data obtained at lower pressures from ultrasonic method with that obtained at higher pressures from the IXS method. Although a discontinuous change in dV_P/dP or in elastic properties at around 10 GPa was suggested by Kawaguchi et al. (2017) who adopted the M-EoS fit, there is no clear evidence of this discontinuous change in our data when we use the 3BM- or V-EoS fits. Thus, we do not consider such discontinuity in this study. The obtained K_{S0} and K'_S of this study from the 3BM- and V-EoS fits are almost comparable (Tables 3 and 4).

The densities of liquid Fe-Ni-S and Fe-Ni-Si are plotted as a function of pressure in Figures 4a and 4b together with previously reported densities. The compression curve of liquid Fe$_{73}$Ni$_{10}$S$_{17}$ in this study agrees with the density reported at 1.8 and 3 GPa (Morard, Garbarino, et al., 2013; Morard, Siebert, et al., 2013) and with the density at ambient pressure extrapolated from data by Nagamori (1969). The density of liquid Fe$_{61}$Ni$_{10}$Si$_{29}$ in this study is located between the compression curves of previous studies (Sanloup et al., 2004; Yu & Secco, 2008). Calculated compression curves using V_P and K_{S0} − K'_S data with equation (2) are drawn in Figure 4. They show an excellent agreement with the density measured by X-ray absorption method. This agreement demonstrates the self-consistency of our experiments in which V_P and ρ were measured independently.

4. Discussion

4.1. The Effect of LEs on the Elastic Properties

The effect of LE on the elastic properties differs significantly depending on alloying LE. Addition of S reduces the K_{S0} of liquid Fe (Anderson & Ahrens, 1994) or Fe-Ni (Kuwabara et al., 2016) from K_{S0}(Fe$_{90}$Ni$_{10}$) = 103 GPa at 1900 K to K_{S0}(Fe$_{60}$Ni$_{10}$S$_{30}$) = 39 GPa at 1650 K, suggesting that the liquid becomes more compressible by adding S even taking into account the different temperature condition. The pressure derivative of the V_P (dV_P/dP) for liquid Fe-Ni-S is larger than those of liquid Fe and Fe-Ni. These elastic features indicate that the V_P of liquid Fe-Ni-S is lower than that of liquid Fe at lower pressures, while it increases rapidly with pressure to be higher than that of liquid Fe at higher pressures (Figure 3a). On the other hand, addition of Si has little

Table 6
Parameters for Equation (5)

| Parameter | Fe-S system | | Fe-Si system | |
	$W_{V(Fe)}$	$W_{V(FeS)}$	$W_{V(Fe)}$	$W_{V(FeSi)}$
a_i	−7.469 ± 0.591	−0.011 ± 0.512	−1.679 ± 0.599	−0.405 ± 0.319
b_i	1.172 ± 0.338	0.875 ± 0.287	0	0

Note. The parameters in this table depend on the EoS of Fe (Anderson & Ahrens, 1994; end member) and should only be used with this EoS.
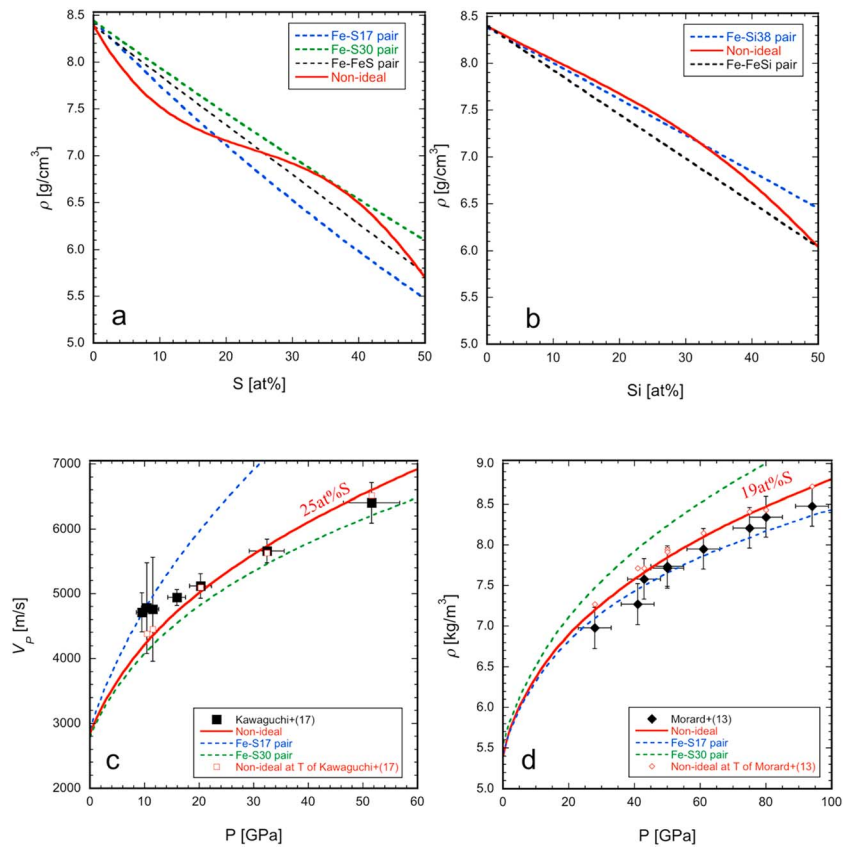
Figure 5. Comparison of mixing models. (a) Density of Fe-Ni-S liquid as a function of S concentration at 25 GPa and 1900 K. The blue, green, and black dashed curves represent ideal solution between Fe-Fe$_{73}$Ni$_{10}$S$_{17}$ (labeled as Fe-S17), Fe-Fe$_{60}$Ni$_{10}$S$_{30}$ (as Fe-S30), and Fe-FeS (labeled as Fe-FeS), respectively. The solid red curve represents the nonideal Fe-FeS solution model of this study. (b) Density of Fe-Ni-Si as a function of Si concentration at 25 GPa and 1900 K. The dashed blue and black curves represent ideal solution between Fe-Fe$_{52}$Ni$_{10}$Si$_{38}$ (labeled as Fe-Si38), and Fe-FeSi (labeled as Fe-FeSi), respectively. The solid red curve represents the nonideal Fe-FeSi solution model of this study. (c) V_P plot as a function of pressure. Calculated V_P of liquid Fe-Ni-S from ideal and nonideal mixing models at 1811 K are shown by dashed blue (Fe-S17) and green (Fe-S30) curves and solid red curve, respectively. Black squares represent V_P data of Fe$_{46.5}$Ni$_{28.5}$S$_{25}$ of Kawaguchi et al. (2017; the composition at 15.9 GPa was Fe$_{63}$Ni$_{12}$S$_{25}$). Red open squares indicate the calculated V_P at the temperature of Kawaguchi et al. (2017). (d) The ρ plot as a function of pressure. Calculated ρ of liquid Fe-Ni-S from ideal and nonideal mixing models at 2300 K are respectively shown by dashed blue or green curves and solid red curve. Black diamonds represent ρ data of Fe$_{76.4}$Ni$_{4.4}$S$_{19.2}$ of Morard, Siebert, et al. (2013). Red open triangles indicate the calculated ρ at the temperature of Morard, Siebert, et al. (2013).

influence on the K_{S0} and K'_S of liquid Fe and Fe-Ni but reduces the density (Table 3). As a result, Si increases the V_P of liquid Fe-Ni only moderately (Figure 3b). Differences in the elastic properties of liquid Fe-Ni-S and Fe-Ni-Si can be well explained by a difference in the local structure of the liquid. S strongly modifies the local structure of liquid Fe, and the poorly ordered structure of liquid Fe-S (Sanloup et al., 2002) induces a large effect on the bulk modulus. In contrast, because Si does not affect the local ordering and the local structure of liquid Fe-Si is similar to that of liquid Fe (Sanloup et al., 2002), Si has only a minor effect on the bulk modulus.

4.2. Mixing Models

In the next step, we need to understand accurate mixing behaviors of liquid Fe-Ni-S and Fe-Ni-Si under pressure for modeling the planetary cores. In previous studies on planetary core modeling, ideal mixing behavior has been assumed to obtain the core thermoelastic properties as a function of LE content. However, the nonideality of the Fe-S and the Fe-Ni-Si systems are suggested from phase relations and density measured at ambient and moderate pressures (Buono & Walker, 2011; Kawai et al., 1974;

Nagamori, 1969; Nishida et al., 2008; Williams et al., 2015), and ab initio calculations at the Earth's core conditions (Alfè et al., 2003). Thus, we examine the effect of different mixing models (ideal and nonideal mixing) on density and V_P for Fe-Ni-S and Fe-Ni-Si liquids in order to assess which model can best summarize the present data.

In a binary mixing model (end member components 1 and 2), the molar volume of the solution mixture (V) is generally given as

$$V = (1-x_2)V_1 + x_2 V_2 + V_{ex} \tag{3}$$

where V_1 and V_2 denote molar volumes of end members 1 and 2 and x_2 is a molar fraction of end member 2. V_{ex} is the excess molar volume (for ideal-mixing case, $V_{ex} = 0$). For the ideal mixing, we consider the following end members: (1) Fe and $Fe_{73}Ni_{10}S_{17}$ or Fe and $Fe_{60}Ni_{10}S_{30}$ for the Fe-Ni-S and (2) Fe and $Fe_{52}Ni_{10}Si_{38}$ for the Fe-Ni-Si. The expressions for the thermoelastic properties in an ideal mixing model are described elsewhere (Rivoldini et al., 2011).

For the nonideal mixing model, an asymmetric Margules formulation (e.g., Buono & Walker, 2011) is adopted. Solution end menbers are set to Fe and FeS for the Fe-S system and Fe and FeSi for the Fe-Si. We assume that the effect of Ni on the mixing can be approximated to that of Fe. The V_1 and V_2 at high pressures and high temperatures are calculated using Vinet EoS with the EoS parameters of the end members listed in Table 5. For the excess molar volume V_{ex}, we have used an asymmetric Margules formulation (Buono & Walker, 2011) written as

$$V_{ex} = x_2 (1-x_2)(x_2 W_{V1} + (1-x_2)W_{V2}) \tag{4}$$

where W_{V1} and W_{V2} are the volume interaction (or Margules) parameters for end members 1 and 2, respectively. The interaction parameters have been obtained by fitting the V_P and ρ data of this study ($Fe_{73}Ni_{10}S_{17}$ and $Fe_{60}Ni_{10}S_{30}$ data for the Fe-Ni-S and $Fe_{61}Ni_{10}Si_{29}$ and $Fe_{52}Ni_{10}Si_{38}$ data for the Fe-Ni-Si) to equations (3) and (4). It is found that the measured V_P and ρ data of this study can be represented correctly with interaction parameters of the following form

$$W_{Vi} = a_i + b_i \log(3/2 + P) \tag{5}$$

where P is pressure in GPa and the a_i and b_i are constants. These constants for end members are given in Table 6. The Grüneisen parameter (γ) of the solution can be calculated from the isobaric heat capacity of the solution; $C_P = (1 - x_2) C_{P1} + x_2 C_{P2}$ (from equation 6 of Buono & Walker, 2011) and by using the thermodynamic identities $\gamma = \frac{\alpha K_S V}{C_P}$ and $K_S = (1 + \alpha \gamma T)K_T$. Then, from the γ of the solution, K_S and $V_P = (K_S/\rho)^{1/2}$ of the solution can be computed.

Calculated densities from ideal and nonideal mixing models are plotted in Figures 5a and 5b at the condition of 25 GPa and 1900 K, an example condition which is near the Martian core-mantle boundary (CMB). For Fe-Ni-S liquid, the ρ of the nonideal mixing model decreases effectively with S than that of ideal mixing models at S < 17 at% (10.5 wt%) and it is bracketed by that of the two ideal mixing (Fe-S17 and Fe-S30) models at S > 17 at% (Figure 5a). For Fe-Ni-Si liquid, density from nonideal mixing is almost consistent with that from ideal mixing in Fe-rich side (up to Si < 30 at%), but it tends to differ in Si-rich side (Si > 30 at%; Figure 5b). Therefore, nonideal mixing behavior is necessary to be considered both for Fe-Ni-S and Fe-Ni-Si systems in order to estimate the elastic properties of Fe-alloys with various S and Si contents. When we extrapolate the V_P and ρ to higher pressures relevant for large planetary cores using both the ideal and nonideal mixing models, the nonideal mixing model well supports recently reported high-pressure data of V_P (Kawaguchi et al., 2017; Figure 5c) and ρ (Morard, Siebert, et al., 2013; Figure 5d). This suggests that the nonideal mixing model combined with Vinet EoS using measured elastic data of this study can accurately link between elastic data obtained at lower pressures and those obtained at higher pressures. This is important when we consider the planetary core which pressure ranges from moderate to high pressures, such as Mercury's core (5–40 GPa) and Martian core (20–40 GPa).

5. Implication to Planetary Cores

Here, we model the planetary cores using the thermoelastic properties of liquid Fe-Ni-S and Fe-Ni-Si alloys to constrain the composition of the cores of Mercury, the Moon, and Mars. To compute the thermo-elastic
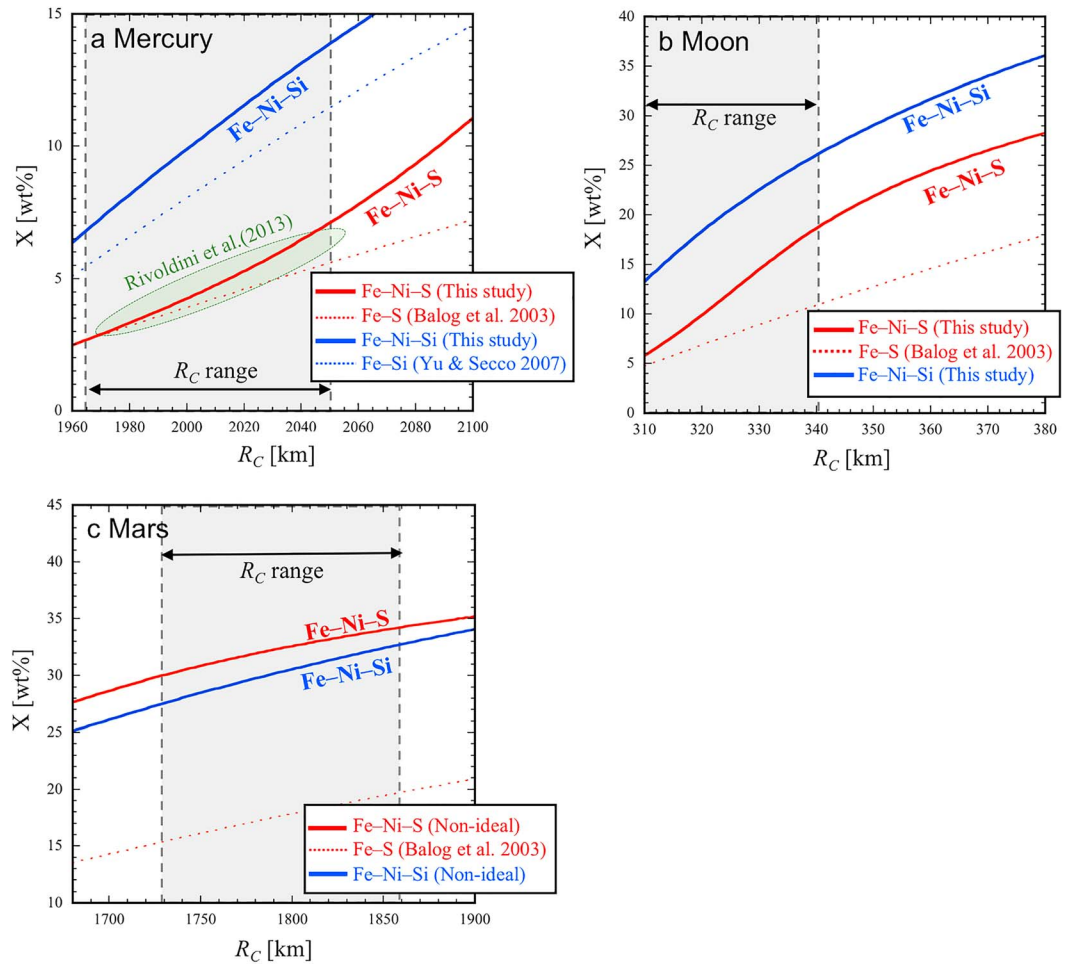
Figure 6. Relations between core radius (R_C) and S or Si content (X) in the core. The results of Fe-Ni-S and Fe-Ni-Si core models are respectively shown in red and blue curves (solid thick curve: elastic data of this study with nonideal mixing model, dotted curve: previous elastic data of Fe-10wt% S (Balog et al., 2003) or that of Fe-17wt% Si (Yu & Secco, 2008) with ideal mixing model). Possible R_C range from MOI and geodesy data are indicated by gray hutch. (a) Mercury's core. Possible R_C range indicated by gray hutch corresponds to 1,965–2,050 km (Mazarico et al., 2014). The green-hatched area indicates the 68% confidence interval for the reported liquid Fe-S core model (Rivoldini & Van Hoolst, 2013). (b) Lunar core. Possible R_C range is 320 ± 20 km (Weber et al., 2011). (c) Martian core. Possible R_C range from the MOI and tidal Love number corresponds to 1,729–1,859 km (Rivoldini et al., 2011).

properties (such as density, bulk modulus, and thermal expansivity) of these alloys, we used the nonideal mixing model for both the Fe-Ni-S and Fe-Ni-Si systems. All models fit the planet mass (M) exactly, and the LE concentration is calculated from the radius and average density of the core. The range of considered core radii is chosen such that it includes the measured mean moment of inertia (MOI). For all models, we assume a silicate shell structure and a liquid core with an adiabatic temperature profile. Details of the interior models of each body are given in Appendix C.

5.1. Mercury's Core

The calculated LE (S or Si) content in the Mercury core is shown as a function of a core radius (R_C) in Figure 6a. The range of core radii plotted in Figure 6a is in accord with measured MOI data (Mazarico et al., 2014; Table C2). To constrain the LE content more precisely, we take a value range for the R_C of 1,965–2,050 km, as estimated from gravity field and spin state data (Hauck et al., 2013; Rivoldini & Van Hoolst, 2013). Our best estimates for the LE content in the core are S = 4.6 + 2.5/−2.0 wt% or Si = 10.5 +3.3/−3.7 wt%. The present estimate of S content is comparable with previously reported S content (4.5 ± 1.8 wt%; Rivoldini & Van Hoolst, 2013). Based on the estimated core compositions, the profiles of V_P and ρ in the
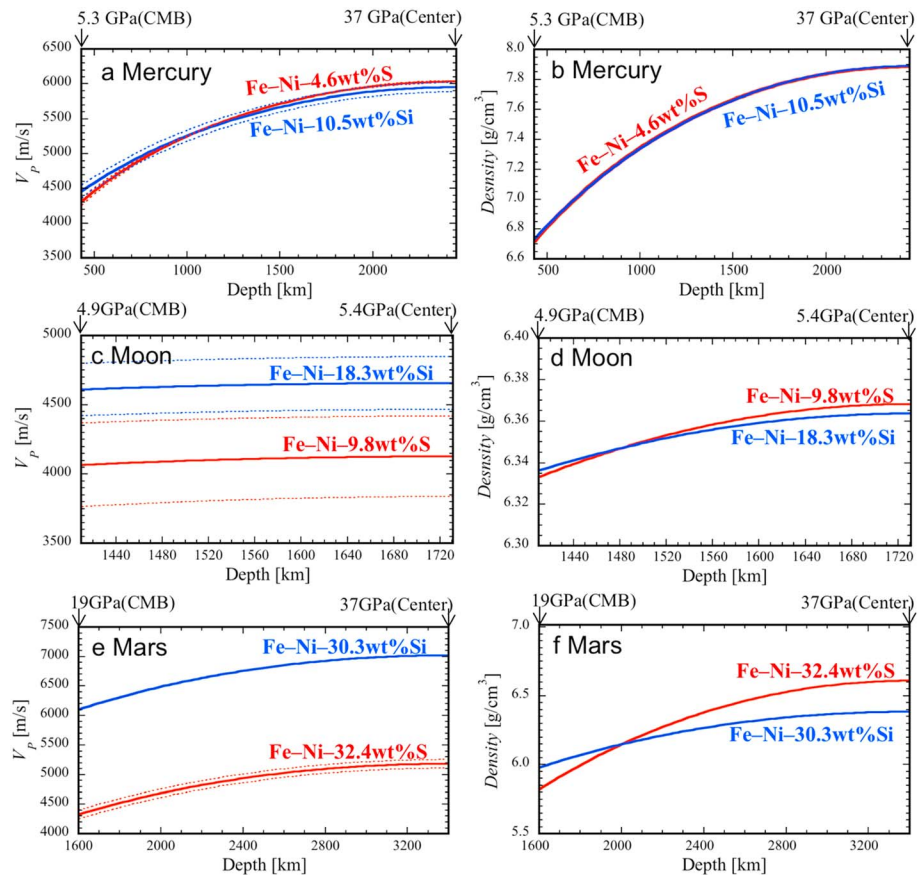
Figure 7. V_P and density profiles of the planetary cores. Red and blue curves respectively represent profiles of Fe-Ni-S and Fe-Ni-Si core. Dotted curves indicate errors of the V_P profile derived from the error of estimated S or Si content. (a,b) Mercury, (c,d) the Moon, and (e,f) Mars.

Mercury molten core are shown in Figures 7a and 7b. The differences in V_P and density between Fe-Ni-4.6wt% S and Fe-Ni-10.5wt% Si are found to be small ($\Delta V_P \sim 150$ m/s, $\Delta\rho \sim 0.01$ g/cm^3) over the entire core range. Even if we take into account the error of LE content, the difference in V_P and ρ between S-rich and Si-rich cores are still small ($\Delta V_P \sim 290$ m/s, $\Delta\rho \sim 0.03$ g/cm^3).

5.2. Lunar Core

The relationship between estimated LE content and core radius (R_C) is shown in Figure 6b. If the R_C of 320 ± 20 km (Weber et al., 2011), deduced from Apollo seismic data, is adopted, the estimated LE concentration in the core is S = 9.8 + 8.8/−7.9 wt% or Si = 18.3 + 7.7/−10.4 wt%. The seismic and density profiles of the lunar core are shown in Figures 7c and 7d. The V_P of an Fe-Ni-S core ranges from 4,070 to 4,130 m/s. The V_P of an Fe-Ni-Si core ranges from 4,610 to 4,660 m/s, which is clearly larger than in a S-rich core. However, the V_P profile of the lunar core has a large uncertainty due to relatively large errors of estimated LE content which derives from R_C error. If the R_C is strictly constrained by geophysical measurements, the V_P profile and thus LE chemistry in the lunar core could be determined. If the outer core V_P of $4,100 \pm 200$ m/s reported by Weber et al. (2011) is adopted, this is consistent with the V_P of Fe-Ni-S core of this study (4,070–4,130 m/s) whereas the V_P of Fe-Ni-Si core (4,610–4,660 m/s) is significantly larger.

5.3. Martian Core

The LE content associated with core radii of Mars are shown in Figure 6c. For $R_C = 1,794 \pm 65$ km, which is estimated from the *MOI* and tidal Love number (Rivoldini et al., 2011), we find that the core contains either 32.4 + 1.8/−2.4 wt% of S or 30.3 + 2.4/−2.8 wt% of Si. This estimation of S concentration is larger than the previous estimates ranging from 14 to 36 wt% (14.2 wt%: Bertka & Fei, 1998;

16.2–17.4 wt%: Sanloup et al., 1999; 20–36 wt%: Zharkov & Gudkova, 2005; 22–25 wt%: Khan & Connolly, 2008; 16 + 1/−2 wt%: Rivoldini et al., 2011). Difference in estimated S amount in the Martian cores between this study and these previous studies results from significant difference between the elastic properties (in particular, density) of Fe-Ni-S of this study and those used in previous studies. The previous estimates of S content used the elastic properties of solid Fe and FeS (Bertka & Fei, 1998; Khan & Connolly, 2008; Sanloup et al., 1999; Zharkov & Gudkova, 2005), or liquid Fe and Fe-10wt%S (Rivoldini et al., 2011). The newly obtained elastic properties of liquid Fe-Ni-S in this study give an important update to the estimation of S content in Martian core. In addition, the present is also larger from chemical composition deduced from Martian meteorite (X_S =14.2 wt%, Dreibus & Wänke, 1985; X_S = 21.4 wt%, Taylor, 2013). If such large fractions of S in the core are discrepant from a geochemical perspective, then S may not be the sole LE in the Martian core.

Note that the liquidus phase of the Martian core, at the compositions found in this study, is either $(Fe,Ni)_{3-x}S_2$ (Fei et al., 2000; Stewart et al., 2007; Urakawa et al., 2018) or $(Fe,Ni)Si$ (Kuwayama & Hirose, 2004) because the S or Si content in the core is richer than the eutectic composition (S = 16 wt% or Si = 25 wt%) at the Martian CMB. These phases will crystallize first and comprise the solid core when the temperature drops below the liquidus. This crystallization scheme will affect dynamo action in the Martian core.

The V_P and ρ profiles of the Martian core are shown in Figures 7e and 7f. The V_P of an Fe-Ni-S core (4,320–5,180 m/s) is much smaller than that of an Fe-Ni-Si core (6,100–7,020 m/s), and the difference is large enough to be detected ($\Delta V_P \sim$ 1,780–1,840 m/s) even if we consider the error in V_P profile. NASA's InSight mission will soon explore the interior structure of Mars through seismic sounding (Banerdt et al., 2013). The seismometers installed on the surface could observe core-interacting body wave phases if the magnitude of seismic events is large enough (Panning et al., 2016). Therefore, by comparing forthcoming seismic data with the present V_P and density profiles, the plausible Martian core composition could be constrained.

6. Conclusions

The effect of pressure, temperature, and composition on sound velocity and density of liquid Fe-Ni-S and Fe-Ni-Si have been measured up to 14 GPa. The pressure dependence of sound velocity is well fitted by using the Birch-Murnaghan or Vinet equation of state. Obtained bulk modulus reduces with increasing S content, whereas it stays constant with variation of Si content. Based on measured elastic properties with the noni-deal mixing model, we estimated the S or Si content in the cores of Mercury (4.6 wt% S or 10.5 wt% Si), the Moon (9.8 wt% S or 18.3 wt% Si), and Mars (32.4 wt% S or 30.3 wt% Si). In the core compositions of Mars and probably Moon, difference in sound velocity between the Fe-Ni-S and Fe-Ni-Si core is large enough to be detected.

In the case that a solid (inner) core exists and the outer core radius is assumed to be constant, LE content in the liquid core is considered as follows. If the core contains less LE than the eutectic composition in total, the LE content in the liquid core is more than that in total molten core because that LE generally partitions into the liquid phase. Hence, the estimated LE content in total molten core corresponds to a lower limit of LE content in the liquid core. In contrast, if the core contains LE more than eutectic composition, LE content in the liquid core would be less than that in total molten core. Thus, the LE content in this study shows upper limit. Mercury and Moon cores correspond to the former case. However, Mars requires much more LE in the core, suggesting that Mars corresponds to the latter case.

The LE contents in planetary cores tend to increase with heliocentric distance, that is, distance from the Sun. This trend highlights the important aspect that the outer terrestrial planet has formed in an environment richer in S or Si, suggesting that chemical zoning or variation in redox state may exist in the early inner solar system.

Appendix A: X-ray CT Measurement

The X-ray radiography image was obtained with a pixel size of 1.43–1.51 μm. The CT measurement was carried out by rotating the press in 0.25–0.50° steps. The exposure time for each image was 150 ms. This setup enables a fast CT measurement (within ~3 min), which is advantageous for molten samples at high temperatures. The volumes of the samples were obtained from vertical stacking of the sample areas in the horizontal

plane. The sample areas were measured, in horizontal cross section image (CT slice), by thresholding the clear contrast between the sample and surrounding BN using image processing software (Image J). The density of the sample was calculated from the sample volume and its weight. The density error estimate is mainly derived from uncertainty in selection of the image processing threshold. Details of density measurement using X-ray CT method are described elsewhere (Kuwabara et al., 2016). As shown in Figure 1a, high temperatures were generated using a cylindrical graphite furnace. Experimental temperatures were estimated from the electric power-temperature relationship at each load condition, which was calibrated in separate experiments with a thermocouple.

Appendix B: Equations of State and Parameter Fitting

B1. Murnaghan EoS

The effect of P on the V_P of liquid Fe-alloys has been expressed with the Murnaghan EoS (Jing et al., 2014). If the bulk modulus, K, is approximated by a linear function of pressure, ρ and K are described as follows (Murnaghan, 1937):

$$P = \frac{K_0}{K_0'}\left[\left(\frac{\rho}{\rho_0}\right)^{K'_0} - 1\right] \tag{B1}$$

$$K = K_0 + K_0'P \tag{B2}$$

where ρ_0, K_0, and K'_0 indicate density, bulk modulus at ambient pressure, and its pressure derivative, respectively.

B2. Birch-Murnaghan EoS

Based on the 3BM EoS, which is widely used for compression behavior of solid materials, P and bulk modulus (K) are described as follows (Birch, 1952):

$$P = \frac{3}{2}K_0\left[\left(\frac{\rho}{\rho_0}\right)^{7/3} - \left(\frac{\rho}{\rho_0}\right)^{5/3}\right]\left\{1 + \frac{3}{4}(K'_0 - 4)\left[\left(\frac{\rho}{\rho_0}\right)^{2/3} - 1\right]\right\}, \tag{B3}$$

$$K = K_0\left(\frac{\rho}{\rho_0}\right)^{5/3}\left[1 + \frac{1}{2}(3K'_0 - 5)\left\{\left(\frac{\rho}{\rho_0}\right)^{2/3} - 1\right\} + \frac{27}{8}(K'_0 - 4)\left\{\left(\frac{\rho}{\rho_0}\right)^{2/3} - 1\right\}^2\right] \tag{B4}$$

where K'_0 is the derivative of the bulk modulus with respect to pressure, and the subscript 0 indicates values at ambient pressure.

B3. Vinet EoS

The Vinet equation is written as (Vinet et al., 1989):

$$P = 3K_0\left(\frac{\rho}{\rho_0}\right)^{2/3}\left[1 - \left(\frac{\rho}{\rho_0}\right)^{-1/3}\right]\exp\left\{\frac{3}{2}(K'_0 - 1)\left[1 - \left(\frac{\rho}{\rho_0}\right)^{-1/3}\right]\right\}, \tag{B5}$$

$$K = \frac{3}{2}K_0\left(\frac{\rho}{\rho_0}\right)^{2/3}\left[\frac{4}{3} + \left(K'_0 - \frac{5}{3}\right)\left(\frac{\rho}{\rho_0}\right)^{-1/3} + (1 - K'_0)\left(\frac{\rho}{\rho_0}\right)^{-2/3}\right]\exp\left\{\frac{3}{2}(1 - K'_0)\left[\left(\frac{\rho}{\rho_0}\right)^{-1/3} - 1\right]\right\}, \tag{B6}$$

The thermal effect on ρ is expressed as

$$\rho_T = \rho_{T0}\exp[-\alpha(T - T_0)], \tag{B7}$$

where ρ_T is ρ at temperature T, and T_0 is reference temperature. The temperature-corrected bulk modulus is calculated as

Table C1

Mercury Mantle Profile

R (km)	P (GPa)	T (K)	ρ (kg/m^3)
2,431	0.1	482	2,900
2,423	0.2	524	2,900
2,414	0.3	566	2,900
2,405	0.4	608	2,900
2,397	0.5	650	3,201
2,388	0.6	692	3,200
2,380	0.7	734	3,198
2,371	0.8	776	3,197
2,362	0.9	818	3,196
2,354	1.0	860	3,195
2,345	1.1	903	3,194
2,336	1.2	945	3,192
2,328	1.3	987	3,191
2,319	1.4	1029	3,190
2,310	1.5	1071	3,189
2,302	1.6	1113	3,187
2,293	1.7	1155	3,186
2,284	1.8	1197	3,185
2,276	1.9	1239	3,183
2,267	2.0	1281	3,182
2,259	2.1	1323	3,181
2,250	2.2	1365	3,179
2,241	2.3	1407	3,178
2,233	2.4	1449	3,176
2,224	2.6	1491	3,175
2,215	2.7	1533	3,174
2,207	2.8	1575	3,172
2,198	2.9	1617	3,171
2,189	3.0	1659	3,169
2,181	3.1	1701	3,168
2,172	3.2	1743	3,166
2,164	3.3	1786	3,165
2,155	3.4	1828	3,163
2,146	3.5	1870	3,162
2,138	3.6	1900	3,162
2,129	3.7	1900	3,165
2,120	3.8	1900	3,169
2,112	3.9	1900	3,172
2,103	4.0	1900	3,175
2,094	4.1	1900	3,179
2,086	4.3	1900	3,182
2,077	4.4	1900	3,186
2,068	4.5	1900	3,189
2,060	4.6	1900	3,192
2,051	4.7	1900	3,196
2,043	4.8	1900	3,199
2,034	4.9	1900	3,202
2,025	5.0	1900	3,206
2,017	5.1	1900	3,209
2,008	5.3	1900	3,212

$$K(\mathrm{P}_0, T) = K_0 \left(\frac{\rho_T}{\rho_{T0}} \right)^{\delta}, \qquad \text{(B8)}$$

where δ represents the Anderson-Grüneisen parameter, $\delta = -(1/\alpha K)(\mathrm{d}K/\mathrm{d}T)_P$ (Anderson, 1967).

For the isothermal settings, V_P and/or ρ data at each *P-T* condition are fitted using a combination of equations of state ((B1), (B3), and (B5)) and finite strain equations ((B2), (B4), and (B6)) taking into account the thermal effect on density (equation (B7)) using the Anderson-Grüneisen relation ($\delta_T = $

Table C2
Models of Mercury Core

R_C (km)	S content (wt%)	MOI
Fe-Ni-S Core Model		
1,960	2.5	0.337094
1,970	2.9	0.338128
1,980	3.3	0.339163
1,990	3.8	0.340200
2,000	4.2	0.341238
2,010	4.7	0.342275
2,020	5.3	0.343312
2,030	5.8	0.344347
2,040	6.4	0.345379
2,050	7.1	0.346406
2,060	7.8	0.347426
2,070	8.5	0.348437
2,080	9.3	0.349437
2,090	10.2	0.350424
2,100	11.1	0.351394
Fe-Ni-Si Core Model		
1,960	6.4	0.337068
1,970	7.3	0.338107
1,980	8.2	0.339151
1,990	9.0	0.340200
2,000	9.9	0.341255
2,010	10.7	0.342316
2,020	11.5	0.343383
2,030	12.3	0.344455
2,040	13.1	0.345533
2,050	13.9	0.346616
2,060	14.6	0.347706
2,070	15.3	0.348801
2,080	16.0	0.349902
2,090	16.7	0.351009
2,100	17.3	0.352122

Note. MOI = moment of inertia.

$-(1/\alpha K_T)(dK_T/dT)_P$. For the fit to V_P, equation (2) and the relation $K_S = (1+\alpha\gamma T)K_T$ was used. As a result of the fitting, K_{T0} and K'_T are obtained together with α_0 and δ_T as listed in Table 4. Since temperature conditions of the data are taken into account in the fitting procedure, no prior temperature correction is applied to the data.

For the isentropic setting, no temperature correction is applied to the data prior to the fitting. To describe V_P and ρ at (P, T) using the elastic parameters, we consider following a P-T path starting from reference conditions (P_0, T_0). In the P-T path for isentropic setting, we start with an isobaric heating at P_0 from T_0 to T_1 (a foot of isentrope), followed by an isentropic compression from (P_0, T_1) to (P, T) with an isentropic EoS for the compression along isentrope. Details of the isentropic setting are described in Verhoeven et al. (2005). All the elastic parameters (K_{S0}, K'_S, ρ_0, α_0, δ_S, and γ) that follow the P-T path described above are estimated simultaneously by fitting the equations describing the isentropic setting to the V_P and ρ data (see Appendix A of Verhoeven et al. (2005) for details). In this study, the elastic parameters (K_{S0}, K'_S, ρ_0, α_0, and δ_S) are obtained from the isentropic fitting as listed in Table 3 assuming fixed γ.

Isothermal and isentropic elastic properties were obtained independently from each fit. To check the consistency between isothermal and isentropic elastic properties, we calculated isentropic K_{S0} and K'_S from obtained K_{T0} and K'_T based on the conversion relation of $K_{S0} = (1+\alpha_0\gamma T)K_{T0}$ using α_0, γ, and T listed in Table 4. The K_{S0} and K'_S obtained from isentropic fit are quite consistent with those calculated from the conversion of isothermal properties, suggesting that elastic properties obtained from isentropic fit and from isothermal fit in this study are consistent each other.

Table C3
Models of Lunar Core

R_C (km)	S content (wt%)	MOI
Fe-Ni-S Core Model		
310	5.8	0.3931131
315	7.7	0.3931153
320	9.8	0.3931176
325	12.2	0.3931200
330	14.5	0.3931223
335	16.7	0.3931248
340	18.7	0.3931272
345	20.4	0.3931297
350	21.9	0.3931322
355	23.2	0.3931347
360	24.5	0.3931373
365	25.5	0.3931400
370	26.5	0.3931426
375	27.4	0.3931453
380	28.3	0.3931480
Fe-Ni-Si Core Model		
310	13.3	0.3931131
315	15.9	0.3931154
320	18.3	0.3931177
325	20.5	0.3931200
330	22.5	0.3931224
335	24.4	0.3931248
340	26.0	0.3931273
345	27.6	0.3931298
350	29.1	0.3931323
355	30.4	0.3931349
360	31.7	0.3931375
365	32.9	0.3931401
370	34.0	0.3931428
375	35.1	0.3931455
380	36.1	0.3931483

Note. MOI = moment of inertia.

Appendix C: Interior Models of Planets

C1. Mercury

Mercury has been considered to have a relatively large core compared with other terrestrial planets. Although sulfur has usually been assumed to be the core LE, a significant amount of silicon could be present in Mercury's core because of the highly reducing formation conditions of Mercury (Nittler et al., 2011). The modeling related to the interior structure of Mercury follows that of previous studies (Dumberry & Rivoldini,

Table C4
Major Element Composition Models of Martian Mantle

Element	DW(85)[a]	MM(03)[b]
CaO	2.4	1.9
FeO	17.9	16.9
MgO	30.2	29.1
Al_2O_3	3.0	2.5
SiO_2	44.4	47.1
Na_2O	0.5	1.2

Note. Numbers correspond to wt%.
[a]Dreibus and Wanke (1985). [b]Mohapatra and Murty (2003).

Table C5
Mars Mantle Profile

R (km)	P (GPa)	T (K)	ρ (kg/m³)
3,358	0.3	446	2,700
3,326	0.6	620	2,700
3,294	1.0	788	3,486
3,262	1.4	930	3,482
3,230	1.8	1062	3,479
3,198	2.2	1184	3,476
3,166	2.6	1298	3,475
3,134	3.0	1401	3,475
3,102	3.4	1496	3,476
3,070	3.8	1581	3,478
3,038	4.2	1656	3,482
3,007	4.6	1722	3,486
2,975	5.0	1779	3,492
2,943	5.4	1818	3,499
2,911	5.8	1827	3,511
2,879	6.2	1835	3,522
2,847	6.6	1844	3,532
2,815	7.0	1853	3,543
2,783	7.4	1862	3,554
2,751	7.7	1871	3,564
2,719	8.1	1879	3,574
2,687	8.5	1888	3,585
2,656	8.9	1897	3,595
2,624	9.3	1906	3,605
2,592	9.7	1914	3,615
2,560	10.1	1923	3,626
2,528	10.4	1932	3,636
2,496	10.8	1941	3,647
2,464	11.2	1950	3,659
2,432	11.6	1958	3,672
2,400	12.0	1967	3,689
2,368	12.3	1976	3,702
2,336	12.7	1985	3,719
2,305	13.1	1994	3,743
2,273	13.5	2002	3,828
2,241	13.9	2011	3,866
2,209	14.3	2020	3,878
2,177	14.7	2029	3,889
2,145	15.1	2038	3,900
2,113	15.5	2046	3,911
2,081	15.8	2055	3,923
2,049	16.2	2064	3,938
2,017	16.6	2073	3,956
1,985	17.0	2081	3,976
1,954	17.4	2090	3,992
1,922	17.8	2099	4,004
1,890	18.2	2108	4,019
1,858	18.6	2117	4,038
1,826	19.0	2125	4,046
1,794	19.4	2134	4,053

2015; Rivoldini & Van Hoolst, 2013). We assumed a thickness of 35 km (Padovan et al., 2015) and an average density of 2,900 kg/cm³ for the crust, and a mixture of olivine (60 wt%) and ortho-pyroxene (40 wt%) for the mantle. The temperature in the mantle is conductive and anchored at the CMB (1900 K) and at the surface (440 K). The density profile of Mercury crust and mantle is listed in Table C1. The calculated results for the Mercury core model are listed in Table C2.

Table C6
Models of Martian Core

R_C (km)	S content (wt%)	MOI
Fe-Ni-S Core Model		
1,700	28.6	0.363143
1,710	29.1	0.363225
1,720	29.6	0.363308
1,730	30.0	0.363392
1,740	30.5	0.363476
1,750	30.9	0.363560
1,760	31.2	0.363645
1,770	31.6	0.363730
1,780	31.9	0.363816
1,790	32.3	0.363902
1,800	32.6	0.363988
1,810	32.9	0.364075
1,820	33.2	0.364162
1,830	33.5	0.364250
1,840	33.7	0.364338
1,850	34.0	0.364426
1,860	34.3	0.364515
1,870	34.5	0.364604
1,880	34.7	0.364693
1,890	35.0	0.364784
1,900	35.2	0.364874
Fe-Ni-Si Core Model		
1,700	26.1	0.363260
1,710	26.6	0.363349
1,720	27.1	0.363439
1,730	27.6	0.363530
1,740	28.0	0.363621
1,750	28.5	0.363713
1,760	28.9	0.363805
1,770	29.3	0.363898
1,780	29.7	0.363991
1,790	30.2	0.364085
1,800	30.6	0.364180
1,810	30.9	0.364274
1,820	31.3	0.364370
1,830	31.7	0.364466
1,840	32.1	0.364563
1,850	32.4	0.364660
1,860	32.8	0.364758
1,870	33.1	0.364856
1,880	33.4	0.364955
1,890	33.8	0.365055
1,900	34.1	0.365156

Note. MOI = moment of inertia.

C2. Moon

Interior structural models of the Moon have been updated recently from high-resolution lunar gravity data (Williams et al., 2014), Apollo seismic data (Garcia et al., 2011; Weber et al., 2011), and a combination thereof (Matsumoto et al., 2015). Taken together, these studies proposed that the Moon's core radius ranges from 200 to 420 km, and with LE, assuming sulfur, below 25 wt%. Here, we model the interior structure of the Moon using the silicate shell structures inferred by Weber et al. (2011), which has been deduced from Apollo seismological data. To have fully liquid cores in our models, the temperature at the CMB was set to 1800 K. The calculated results of the lunar core model are listed in Table C3.

C3. Mars

Because seismic measurements for Mars are not yet available, constraints on interior structure models of Mars are usually obtained from geodesy data and assumptions of the planet's thermal state and composition (Sohl & Spohn, 1997; Zharkov & Gudkova, 2000; Urakawa et al., 2004; Khan & Connolly, 2008; Rivoldini et al., 2011). Bulk composition models of Mars deduced from Martian meteorites show that sulfur is likely the most abundant LE in its core (Dreibus & Wänke, 1985). Other LEs that could be present, together with sulfur, in smaller amounts are hydrogen (Zharkov & Gudkova, 2000) and silicon (Mohapatra & Murty, 2003).

Here, we consider two model settings for the Martian core and mantle composition: (i) an Fe-Ni-S core with the mantle composition suggested by Dreibus and Wänke (1985) and (ii) an Fe-Ni-Si core with the mantle composition suggested by Mohapatra and Murty (2003). The mantle compositions according to these models are listed in Table C4. Mantle mineralogies for the two compositions have been computed with the Perple_X program (Connolly, 2009) using thermodynamic data derived by Stixrude and Lithgow-Bertelloni (2011). The crust thickness and average density were fixed to 55 km and 2,700 kg/cm^3 (Wieczorek & Zuber, 2004). We have adopted a temperature profile of the mantle deduced from a recent study about the thermal evolution of Mars (Case 21 in Plesa et al., 2016) and set the temperature at the CMB to 2105–2160 K, depending on the R_C. For these models, we provide a range of core radii and compositions that agree with the most recent mass and MOI estimates of Mars (Konopliv et al., 2016). The density profile of Martian crust and mantle is listed in Table C5. The calculated results of the Martian core models are listed in Table C6.

References

Alfè, D., Gillan, M. J., & Price, G. D. (2003). Thermodynamics from first principles: Temperature and composition of the Earth's core. *Mineralogical Magazine*, *67*(1), 113–123. https://doi.org/10.1180/0026461026610089

Anderson, O. L. (1967). Equation for thermal expansivity in planetary interiors. *Journal of Geophysical Research*, *72*(14), 3661–3668. https://doi.org/10.1029/JZ072i014p03661

Anderson, W. W., & Ahrens, T. J. (1994). An equation of state for liquid iron and implications for the Earth's core. *Journal of Geophysical Research*, *99*(B3), 4273–4284. https://doi.org/10.1029/93JB03158

Antonangeli, D., Morard, G., Schmerr, N. C., Komabayashi, T., Krisch, M., Fiquet, G., & Fei, Y. (2015). Toward a mineral physics reference model for the Moon's core. *Proceedings of the National Academy of Sciences of the United States of America*, *112*(13), 3916–3919. https://doi.org/10.1073/pnas.1417490112

Balog, P. S., Secco, R. A., Rubie, D. C., & Frost, D. J. (2003). Equation of state of liquid Fe-10 wt % S: Implications for the metallic cores of planetary bodies. *Journal of Geophysical Research*, *108*(B2), 2124. https://doi.org/10.1029/2001JB001646

Banerdt, W. B., Smrekar, S., Lognonné, P., Spohn, T., Asmar, S. W., Banfield, D., et al. (2013). INSIGHT: A discovery mission to explore the interior of Mars. *44th Lunar Planet Sci Conf* abstract, 1915

Bertka, C. M., & Fei, Y. (1998). Density profile of and SNC model Martian interior and the moment-of-inertia factor of Mars. *Earth and Planetary Science Letters*, *157*(1-2), 79–88. https://doi.org/10.1016/S0012-821X(98)00030-2

Birch, F. (1952). Elasticity and constitution of the Earth's interior. *Journal of Geophysical Research*, *57*(2), 227–286. https://doi.org/10.1029/JZ057i002p00227

Brearley, A. J., & Jones, R. H. (1998). Chondritic meteorites. In J. J. Papike (Ed.), *Planetary materials*, *Reviews in Mineralogy*, (Vol. 36, pp. 3-1–3-398). Washington DC: Mineralogical Society of America.

Buono, A. S., & Walker, D. (2011). The Fe-rich liquidus in the Fe-FeS system from 1 bar to 10 GPa. *Geochimica et Cosmochimica Acta*, *75*(8), 2072–2087. https://doi.org/10.1016/j.gca.2011.01.030

Cohen, R. E., Gulseren, O., & Hemley, R. J. (2000). Accuracy of equation-of-state formulations. *American Mineralogist*, *85*(2), 338–344. https://doi.org/10.2138/am-2000-2-312

Connolly, J. A. D. (2009). The geodynamic equation of state: What and how. *Geochemistry, Geophysics, Geosystems*, *10*, Q10014. https://doi.org/10.1029/2009gc002540

Dreibus, G., & Wänke, H. (1985). Mars, a volatile-rich planet. *Meteoritics*, *20*, 367–381.

Dumay, C., & Cramb, A. W. (1995). Density and interfacial tension of liquid Fe–Si alloys. *Metallurgical and Materials Transactions B*, *26B*, 173–176. https://doi.org/10.1007/bf02648989

Dumberry, M., & Rivoldini, A. (2015). Mercury's inner core size and core-crystallization regime. *Icarus*, *248*, 254–268. https://doi.org/10.1016/j.icarus.2014.10.038

Fei, Y., Li, J., Bertka, C. M., & Prewitt, C. T. (2000). Structure and bulk modulus of Fe$_3$S, a new iron-sulfur compound. *American Mineralogist*, *85*(11-12), 1830–1833. https://doi.org/10.2138/am-2000-11-1229

Garcia, R., Gagnepain-Beyneix, J., Chevrot, S., & Lognonné, P. (2011). Very preliminary reference Moon model. *Physics of the Earth and Planetary Interiors*, *188*(1-2), 96–113. https://doi.org/10.1016/j.pepi.2011.06.015

Hauck, S. A. II, Margot, J. L., Solomon, S. C., Phillips, R. J., Johnson, C. L., Lemoine, F. G., et al. (2013). The curious case of Mercury's internal structure. *Journal of Geophysical Research: Planets*, *118*, 1204–1220. https://doi.org/10.1002/jgre.20091

Higo, Y., Kono, Y., Inoue, T., Irifune, T., & Funakoshi, K. (2009). A system for measuring elastic wave velocity under high pressure and high temperature using a combination of ultrasonic measurement and the multi-anvil apparatus at SPring-8. *Journal of Synchrotron Radiation*, *16*(6), 762–768. https://doi.org/10.1107/S0909049509034980

Javoy, M., Kaminski, E., Guyot, F., Andrault, D., Sanloup, C., Moreira, M., et al. (2010). The chemical composition of the Earth: Enstatite chondrite models. *Earth and Planetary Science Letters*, *293*(3-4), 259–268. https://doi.org/10.1016/j.epsl.2010.02.033

Jing, Z., Wang, Y., Kono, Y., Yu, T., Sakamaki, T., Park, C., et al. (2014). Sound velocity of Fe–S liquids at high pressure: Implications for the Moon's molten outer core. *Earth and Planetary Science Letters*, *396*, 78–87. https://doi.org/10.1016/j.epsl.2014.04.015

Kaiura, G. H., & Toguri, J. M. (1979). Densities of the molten FeS, FeS-CuS₂ and Fe-S-O systems-Utilizing a bottom-balance Archimedean technique. *Canadian Metallurgical Quarterly*, *18*(2), 155–164. https://doi.org/10.1179/cmq.1979.18.2.155

Katayama, Y. (1996). Density measurements of non-crystalline materials under high pressure and high temperature. *High Pressure Research*, *14*(4-6), 383–391. https://doi.org/10.1080/08957959608201424

Kawaguchi, I. S., Nakajima, Y., Hirose, K., Komabayashi, T., Ozawa, H., Tateno, S., et al. (2017). Sound velocity of liquid Fe-Ni-S at high pressure. *Journal of Geophysical Research: Solid Earth*, *122*, 3624–3634. https://doi.org/10.1002/2016JB013609

Kawai, Y., Mori, K., Kishimoto, M., Ishikura, K., & Shimoda, S. (1974). Surface tension of liquid Fe-C-Si alloys (In Japanese text with English abstract). *Tetsu to Hagane*, *60*(1), 29–37. https://doi.org/10.2355/tetsutohagane1955.60.1_29

Khan, A., & Connolly, J. A. D. (2008). Constraining the composition and thermal state of Mars from inversion of geophysical data. *Journal of Geophysical Research*, *113*(E7), E07003. https://doi.org/10.1029/2007JE002996

Kono, Y., Park, C., Sakamaki, T., Kenny-Benson, C., Shen, G., & Wang, Y. (2012). Simultaneous structure and elastic wave velocity measurement of SiO₂ glass at high pressures and high temperatures in a Paris-Edinburgh cell. *The Review of Scientific Instruments*, *83*, 033905. https://doi.org/10.1063/1.3698000

Konopliv, A. S., Park, R. S., & Folkner, W. M. (2016). An improved JPL Mars gravity field and orientation from Mars orbiter and lander tracking data. *Icarus*, *274*, 253–260. https://doi.org/10.1016/j.icarus.2016.02.052

Kuwabara, S., Terasaki, H., Nishida, K., Shimoyama, Y., Takubo, Y., Higo, Y., et al. (2016). Sound velocity and elastic properties of Fe–Ni and Fe–Ni–C liquids at high pressure. *Physics and Chemistry of Minerals*, *43*(3), 229–236. https://doi.org/10.1007/s00269-015-0789-y

Kuwayama, Y., & Hirose, K. (2004). Phase relations in the system Fe-FeSi at 21 GPa. *American Mineralogist*, *89*(2-3), 273–276. https://doi.org/10.2138/am-2004-2-303

Malavergne, V., Toplis, M. J., Berthet, S., & Jones, J. (2010). Highly reducing conditions during core formation on Mercury: Implications for internal structure and the origin of a magnetic field. *Icarus*, *206*(1), 199–209. https://doi.org/10.1016/j.icarus.2009.09.001

Margot, J. L., Peale, S. J., Jurgens, R. F., Slade, M. A., & Holin, I. V. (2007). Large longitude libration of Mercury reveals a molten core. *Science*, *316*(5825), 710–714. https://doi.org/10.1126/science.1140514

Matsui, M. (2009). Temperature-pressure-volume equation of state of the B1 phase of sodium chloride. *Physics of the Earth and Planetary Interiors*, *174*(1-4), 93–97. https://doi.org/10.1016/j.pepi.2008.05.013

Matsumoto, K., Yamada, R., Kikuchi, F., Kamata, S., Ishihara, Y., Iwata, T., et al. (2015). Internal structure of the Moon inferred from Apollo seismic data and selenodetic data from GRAIL and LLR. *Geophysical Research Letters*, *42*, 7351–7358. https://doi.org/10.1002/2015GL065335

Mazarico, E., Genova, A., Goossens, S., Lemoine, F. G., Neumann, G. A., Zuber, M. T., et al. (2014). The gravity field, orientation, and ephemeris of Mercury from MESSENGER observations after three years in orbit. *Journal of Geophysical Research: Planets*, *119*, 2417–2436. https://doi.org/10.1002/2014JE004675

Mittlefehldt, D. W., McCoy, T. J., Goodrich, C. A., & Kracher, A. (1998). Non-chondritic meteorites from asteroidal bodies. In J. J. Papike (Ed.), *Planetary materials*, *Reviews in Mineralogy*, (Vol. 36, pp. 4-1–4-195). Washington DC: Mineralogical Society of America.

Mohapatra, R. K., & Murty, S. V. S. (2003). Precursors of Mars: Constraints from nitrogen and oxygen isotopic compositions of martian meteorites. *Meteoritics and Planetary Science*, *38*(2), 225–241. https://doi.org/10.1111/j.1945-5100.2003.tb00261.x

Morard, G., Garbarino, G., Antonangeli, D., Andrault, D., Guignot, N., Siebert, J., et al. (2013). Density measurements and structural properties of liquid and amorphous metals under high pressure. *High Pressure Research*, *34*(1), 9–21. https://doi.org/10.1080/08957959.2013.860137

Morard, G., Siebert, J., Andrault, D., Guignot, N., Garbarino, G., Guyot, F., & Antonangeli, D. (2013). The Earth's core composition from high pressure density measurements of liquid iron alloys. *Earth and Planetary Science Letters*, *373*, 169–178. https://doi.org/10.1016/j.epsl.2013.04.040

Murnaghan, F. D. (1937). Finite deformation of an elastic solid. *American Journal of Mathematics*, *59*(2), 235–260. https://doi.org/10.2307/2371405

Nagamori, M. (1969). Density of molten Ag-S, Cu-S, Fe-S, and Ni-S systems. *Transactions of the Metallurgical Society of the American Institute of Mechanical Engineers*, *245*, 1897–1902.

Nakajima, Y., Imada, S., Hirose, K., Komabayashi, T., Ozawa, H., Tateno, S., et al. (2015). Carbon-depleted outer core revealed by sound velocity measurements of liquid iron-carbon alloy. *Nature Communications*, *6*, 8942. https://doi.org/10.1038/ncomms9942

Nasch, P. M., Manghnani, M. H., & Secco, R. A. (1997). Anomalous behavior of sound velocity and attenuation in liquid Fe–Ni–S. *Science*, *277*(5323), 219–221. https://doi.org/10.1126/science.277.5323.219

Nishida, K., Kono, Y., Terasaki, H., Takahashi, S., Ishii, M., Shimoyama, Y., et al. (2013). Sound velocity measurements in liquid Fe–S at high pressure: Implications for Earth's and lunar cores. *Earth and Planetary Science Letters*, *362*, 182–186. https://doi.org/10.1016/j.epsl.2012.11.042

Nishida, K., Suzuki, A., Terasaki, H., Shibazaki, Y., Higo, Y., Kuwabara, S., et al. (2016). Towards a consensus on the pressure and composition dependence of sound velocity in the liquid Fe-S system. *Physics of the Earth and Planetary Interiors*, *257*, 230–239. https://doi.org/10.1016/j.pepi.2016.06.009

Nishida, K., Terasaki, H., Ohtani, E., & Suzuki, A. (2008). The effect of sulphur content on density of the liquid Fe-S at high pressure. *Physics and Chemistry of Minerals*, *35*(7), 417–423. https://doi.org/10.1007/s00269-008-0236-4

Nittler, L. R., Starr, R. D., Weider, S. Z., McCoy, T. J., Boynton, W. V., Ebel, D. S., et al. (2011). The major-element composition of Mercury's surface from MESSENGER X-ray spectrometry. *Science*, *333*(6051), 1847–1850. https://doi.org/10.1126/science.1211567

Padovan, S., Wieczorek, M. A., Margot, J.-L., Tosi, N., & Solomon, S. C. (2015). Thickness of the crust of Mercury from geoid-to-topography ratios. *Geophysical Research Letters*, *42*, 1029–1038. https://doi.org/10.1002/2014GL062487

Palme, H., & Jones, A. (2005). Solar system abundances of the elements. In A. M. Davis (Ed.) *Meteorites, comets, and planets*, Vol. 1, H. D. Holland, & K. K. Turekian (Eds.) *Treatise on Geochemistry*, Oxford, Elsevier-Pergamon, pp. 41–61.

Panning, M. P., Lognonné, P., Bruce Banerdt, W., Garcia, R., Golombek, M., Kedar, S., et al. (2016). Planned products of the Mars Structure Service for the InSight mission to Mars. *Space Science Reviews*, *211*(1-4), 611–650. https://doi.org/10.1007/s11214-016-0317-5

Plesa, A.-C., Grott, M., Tosi, N., Breuer, D., Spohn, T., & Wieczorek, M. A. (2016). How large are present-day heat flux variations across the surface of Mars? *Journal of Geophysical Research: Planets*, *121*, 2386–2403. https://doi.org/10.1002/2016JE005126

Rivoldini, A., & Van Hoolst, T. (2013). The interior structure of Mercury constrained by the low-degree gravity field and the rotation of Mercury. *Earth and Planetary Science Letters*, *377-378*, 62–72. https://doi.org/10.1016/j.epsl.2013.07.021

Rivoldini, A., Van Hoolst, T., Verhoeven, O., Mocquet, A., & Dehant, V. (2011). Geodesy constraints on the interior structure and composition of Mars. *Icarus*, *213*(2), 451–472. https://doi.org/10.1016/j.icarus.2011.03.024

Rubie, D. C., Jacobson, S. A., Morbidelli, A., O'Brien, D. P., Young, E. D., de Vries, J., et al. (2015). Accretion and differentiation of the terrestrial planets with implications for the compositions of early-formed Solar System bodies and accretion of water. *Icarus*, *248*, 89–108. https://doi.org/10.1016/j.icarus.2014.10.015

Sanloup, C., Fiquet, G., Gregoryanz, E., Morard, G., & Mezouar, M. (2004). Effect of Si on liquid Fe compressibility: Implications for sound velocity in core materials. *Geophysical Research Letters*, *31*, L07604. https://doi.org/10.1029/2004GL019526

Sanloup, C., Guyot, F., Gillet, P., & Fei, Y. (2002). Physical properties of liquid Fe alloys at high pressure and their bearings on the nature of metallic planetary cores. *Journal of Geophysical Research*, *107*(B11), ECV 4-1–ECV 4-9. https://doi.org/10.1029/2001JB000808

Sanloup, C., Guyot, F., Gillet, P., Fiquet, G., Mezouar, M., & Martinez, I. (2000). Density measurements of liquid Fe-S at high-pressure. *Geophysical Research Letters*, *27*(6), 811–814. https://doi.org/10.1029/1999GL008431

Sanloup, C., Jambon, A., & Gillet, P. (1999). A simple chondritic model of Mars. *Physics of the Earth and Planetary Interiors*, *112*(1-2), 43–54. https://doi.org/10.1016/S0031-9201(98)00175-7

Shimoyama, Y., Terasaki, H., Urakawa, S., Takubo, Y., Kuwabara, S., Kishimoto, S., et al. (2016). Thermoelastic properties of liquid Fe-C revealed by sound velocity and density measurements at high pressure. *Journal of Geophysical Research: Solid Earth*, *121*, 7984–7995. https://doi.org/10.1002/2016JB012968

Shobu, T., Tozawa, K., Shiwaku, H., Konishi, H., Inami, T., Harami, T., & Mizuki, J. (2007). Wide band energy beamline using Si(111) crystal monochromaters at BL22XU in SPring-8. *AIP Conference Proceedings*, *879*, 902. https://doi.org/10.1063/1.2436207

Smith, D. E., Zuber, M. T., Phillips, R. J., Solomon, S. C., Hauck, S. A., Lemoine, F. G., et al. (2012). Gravity field and internal structure of Mercury from MESSENGER. *Science*, *336*(6078), 214–217. https://doi.org/10.1126/science.1218809

Sohl, F., & Spohn, T. (1997). The interior structure of Mars: Implications from SNC meteorites. *Journal of Geophysical Research*, *102*(E1), 1613–1635. https://doi.org/10.1029/96JE03419

Steenstra, E. S., Rai, N., Knibbe, J. S., Lin, Y. H., & van Westrenen, W. (2016). New geochemical models of core formation in the Moon from metal–silicate partitioning of 15 siderophile elements. *Earth and Planetary Science Letters*, *441*, 1–9. https://doi.org/10.1016/j.epsl.2016.02.028

Stewart, A. J., Schmidt, M. W., van Westrenen, W., & Liebske, C. (2007). Mars: A new core-crystallization regime. *Science*, *316*(5829), 1323–1325. https://doi.org/10.1126/science.1140549

Stixrude, L., & Lithgow-Bertelloni, C. (2011). Thermodynamics of mantle minerals—II. Phase equilibria. *Geophysical Journal International*, *184*(3), 1180–1213. https://doi.org/10.1111/j.1365-246X.2010.04890.x

Suzuki, Y., Uesugi, K., Takimoto, N., Fukui, T., Aoyama, K., Takeuchi, A., et al.(2004). Construction and commissioning of A 248 m-long beamline with X-ray undulator light source. *AIP Conference Proceedings*, *705*, 344. https://doi.org/10.1063/1.1757804

Tange, Y., Nishihara, Y., & Tsuchiya, T. (2009). Unified analyses for *P-V-T* equation of state of MgO: A solution for pressure-scale problems in high *P-T* experiments. *Journal of Geophysical Research*, *114*, B03208. https://doi.org/10.1029/2008JB005813

Taylor, G. J. (2013). The bulk composition of Mars. *Chemie der Erde*, *73*(4), 401–420. https://doi.org/10.1016/j.chemer.2013.09.006

Terasaki, H., Nishida, K., Urakawa, S., Takubo, Y., Kuwabara, S., Shimoyama, Y., et al. (2019). Sound velocity and density of liquid $Ni_{68}S_{32}$ under pressure using ultrasonic and X-ray absorption with tomography methods. *Comptes Rendus Geoscience*, *351*(2-3), 163–170. https://doi.org/10.1016/j.crte.2018.04.005

Tsuchiya, T. (2003). First-principles prediction of the *P-V-T* equation of state of gold and the 660-km discontinuity in Earth's mantle. *Journal of Geophysical Research*, *108*(B10), B102463. https://doi.org/10.1029/2003JB002446

Urakawa, S., Kamuro, R., Suzuki, A., & Kikegawa, T. (2018). Phase relationships of the system Fe–Ni–S and structure of the high-pressure phase of $(Fe_{1-x}Ni_x)_3S_2$. *Physics of the Earth and Planetary Interiors*, *277*, 30–37. https://doi.org/10.1016/j.pepi.2018.01.007

Urakawa, S., Someya, K., Terasaki, H., Katsura, T., Yokoshi, S., Funakoshi, K., et al. (2004). Phase relationships and equations of state for FeS at high pressures and high temperatures and implications to the internal structure of Mars. *Physics of the Earth and Planetary Interiors*, *143-144*, 469–479. https://doi.org/10.1016/j.pepi.2003.12.015

Urakawa, S., Terasaki, H., Funakoshi, K., Uesugi, K., & Yamamoto, S. (2010). Development of high pressure apparatus for X-ray micro-tomography at SPring-8. *Journal of Physics Conference Series*, *215*, 012026. https://doi.org/10.1088/1742-6596/215/1/012026

Verhoeven, O., Rivoldini, A., Vacher, P., Mocquet, A., Choblet, G., Menvielle, M., et al. (2005). Interior structure of terrestrial planets: Modeling Mars' mantle and its electromagnetic, geodetic, and seismic properties. *Journal of Geophysical Research*, *110*, E04009. https://doi.org/10.1029/2004JE002271

Vinet, P., Rose, J. H., Ferrante, J., & Smith, J. R. (1989). Universal features of the equation of state of solids. *Journal of Physics. Condensed Matter*, *1*, 1941–1963. https://doi.org/10.1088/0953-8984/1/11/002

Wakabayashi, D., & Funamori, N. (2015). Solving the problem of inconsistency in the reported equations of state for h–BN. *High Pressure Research*, *35*(2), 123–129. https://doi.org/10.1080/08957959.2015.1028931

Wasson, J. T. (1989). The building stones of the planets. In F. Vilas, C. R. Chapman, & M. S. Matthews (Eds.), *Mercury*, (pp. 622–650). Tucson: University of Arizona Press.

Weber, R. C., Lin, P.-Y., Garnero, E. J., Williams, Q., & Lognonné, P. (2011). Seismic detection of the lunar core. *Science*, *331*(6015), 309–312. https://doi.org/10.1126/science.1199375

Wieczorek, M. A., & Zuber, M. T. (2004). Thickness of the Martian crust: Improved constraints from geoid-to-topography ratios. *Journal of Geophysical Research*, *109*(E1), E01009. https://doi.org/10.1029/2003JE002153

Williams, J. G., Boggs, D. H., Yoder, C. F., Ratcliff, J. T., & Dickey, J. O. (2001). Lunar rotational dissipation in solid body and molten core. *Journal of Geophysical Research*, *106*(E11), 27,933–27,968. https://doi.org/10.1029/2000JE001396

Williams, J. G., Konopliv, A. S., Boggs, D. H., Park, R. S., Yuan, D. N., Lemoine, F. G., et al. (2014). Lunar interior properties from the GRAIL mission. *Journal of Geophysical Research: Space Physics*, *119*, 1546–1578. https://doi.org/10.1002/2013JE004559

Williams, Q., Manghnani, M. H., Secco, R. A., & Fu, S. (2015). Limitations on silicon in the outer core: Ultrasonic measurements at high temperatures and high d*K*/d*P* values of Fe-Ni-Si liquids at high pressures. *Journal of Geophysical Research: Solid Earth*, *120*, 6846–6855. https://doi.org/10.1002/2015JB012270

Yoder, C. F., Konopliv, A. S., Yuan, D. N., Standish, E. M., & Folkner, W. M. (2003). Fluid core size of Mars from detection of the solar tide. *Science*, *300*(5617), 299–303. https://doi.org/10.1126/science.1079645

Yu, X., & Secco, R. A. (2008). Equation of state of liquid Fe–17 wt%Si to 12GPa. *High Pressure Research*, *28*(1), 19–28. https://doi.org/10.1080/08957950701882138

Zharkov, V. N., & Gudkova, T. V. (2000). Interior structure models, Fe/Si ratio and parameters of figure for Mars. *Physics of the Earth and Planetary Interiors*, *117*(1-4), 407–420. https://doi.org/10.1016/S0031-9201(99)00110-7

Zharkov, V. N., & Gudkova, T. V. (2005). Construction of Martian interior model. *Solar System Research*, *39*(5), 343–373. https://doi.org/10.1007/s11208-005-0049-7